Sea surface height anomaly and geostrophic current velocity from altimetry measurements over the Arctic Ocean (2011-2020)

Francesca Doglioni[1], Robert Ricker[1], Benjamin Rabe[1], Alexander Barth[2], Charles Troupin[2], and Torsten Kanzow[1,3]

[1]Alfred Wegener Institute, Helmholtz Centre for Polar and Marine Research, Bremerhaven, Germany.
[2]GeoHydrodynamics and Environment Research (GHER), University of Liège, Belgium.
[3]Department 1 of Physics and Electrical Engineering, University of Bremen, Germany.

Correspondence: Francesca Doglioni (francesca.doglioni@awi.de)

Abstract.

Satellite altimetry missions flying over the ice-covered Arctic opened the possibility to further understand changes in the ocean beneath the sea ice. This requires complex processing of satellite signals emerging from leads within the sea ice, with efforts to generate consistent Arctic-wide datasets ongoing. The aim of this paper is to provide and assess a novel gridded

5 dataset of sea surface height anomaly and geostrophic velocity, which incorporates both the ice-covered and open ocean areas of the Arctic. Data from the Cryosat-2 mission in the period 2011-2020 were gridded at one month intervals, up to 88° N, using the Data-Interpolating Variational Analysis (DIVA) method. To examine the robustness of our results, we compare our dataset to independent satellite and in-situ data. We find that our dataset is well correlated with independent satellite data at monthly time scales and agrees with in-situ observed variability at seasonal to interannual time scales. Our geostrophic velocity fields

10 can resolve the variability of boundary currents wider than about 50 km. Large scale seasonal features emerge: a wintertime Arctic-wide maximum in sea surface height, with the highest amplitude over the shelves, and basin wide seasonal acceleration of Arctic slope currents in winter. We suggest that this dataset can be used to study not only the large scale sea surface height and circulation but also the regionally confined boundary currents.

1   Introduction

15 Regionally enhanced atmospheric warming in the Arctic over the past century has been driving rapid changes at the sea surface. The reduction in concentration and age of sea ice resulted in modified vertical momentum fluxes, which intensified ice and water drift, in turn enhancing sea ice drift and export. Evidence of basin-wide positive trends in sea ice drift, particularly strong in the summer season, has largely been found in satellite observations (Hakkinen et al., 2008; Spreen et al., 2011; Kwok et al., 2013; Kaur et al., 2018). Contrary to studies on ice drift, observational studies of ocean currents give a more fragmentary

20 picture of changes and intensification of surface ocean currents: analysis of regional in situ data (e.g., McPhee, 2012), indirect calculation from wind and ice drift observation (Ma et al., 2017) or, only recently, satellite altimetry data (Armitage et al., 2017; Morison et al., 2021). The reason for this is that, in ice covered regions, long-term observation of near surface currents, either from in situ or satellite sensors, has been hindered until recent times by the very presence of ice.

Before the advent of satellite observations, the large scale Arctic Ocean surface circulation (see a schematic in Fig. 1) was
partially reconstructed from in-situ observations and models, albeit with limitations in terms of spatial extent or processes
represented. On the one hand, in-situ observations of surface ocean currents are sparse due to the remoteness of the Arctic
environment and to the high risk of loosing sensors in ice-covered areas (Haller et al., 2014). On the other hand, while numerical
models allow for the study of basin-wide processes, they rely largely on theoretical formulation of physical processes, often
constrained by insufficient in-situ observations (Proshutinsky and Johnson, 1997; Jahn et al., 2010). Satellite-derived data then
provided novel alternatives to tackle these issues. For instance, based on assumptions of the ice response to wind forcing (i.e.,
free drift), Kwok et al. (2013) used satellite sea ice drift observations to deduce near-surface ocean circulation. Beyond ice drift
observations, satellite altimetry can provide a more direct way to observe near-surface ocean currents (Armitage et al., 2017).
This is because altimetry derived sea surface height can be used to compute the geostrophic velocity, a component of the ocean
surface velocity which is dominant in the Arctic on spatial scales larger than ten kilometres (Nurser and Bacon, 2014) and time
scales longer than a few days.

The first satellite altimetry missions over the Arctic ocean, launched in the 90s and at the turn of the 21st century, covered
it only partially up to 82° N (e.g., ERS 1 and 2, Envisat), or flew over ice regions for limited periods of time (ICEsat-1).
Cryosat-2 is currently the mission providing the most complete coverage and longest life span, with observations up to 88° N
since 2010 (Wingham et al., 2006). Further data are provided by recently launched missions, such as Sentinel-3 and ICEsat-2.
Despite the availability of data, methodological developments for the processing of the signal coming from the ocean in ice-
covered regions have taken much longer to develop. The observations were originally aimed at the study of the cryosphere
(Laxon, 1994; Alexandrov et al., 2010; Ricker et al., 2014; Armitage and Davidson, 2014), with efforts towards the generation
of altimetric datasets for oceanographic purposes being made later (e.g., Bouffard et al., 2017). For this reason, many available
oceanographic datasets are limited either to the open ocean (Volkov and Pujol, 2012; Müller et al., 2019) or to the ice-covered
ocean (Kwok and Morison, 2011, 2016; Mizobata et al., 2016).

Only in the past years have few basin-wide, multi-annual, gridded datasets of sea surface height been generated at monthly
timescales (Armitage et al., 2016; Rose et al., 2019; Prandi et al., 2021). These datasets play an important role in improving
our understanding of the Arctic system as a whole, and of its present and future change (Timmermans and Marshall, 2020).
However, differences between them are introduced by the altimeter signal processing (Ricker et al., 2014; Armitage and David-
son, 2014; Passaro et al., 2014), measurements corrections (Carrère et al., 2016; Ricker et al., 2016; Birol et al., 2017) and/or
interpolation of observations onto regular grids. Yet, it is not well known how these products compare to each other, nor to
what extent their spatial and temporal resolution is robust in ice covered regions (e.g., noise to signal ratio). Sea surface height
maps have been assessed mostly against tide gauge data at the periphery of the Arctic Ocean, or in ice-covered regions against
data from hydrographic profiles, which makes it difficult to evaluate the robustness of monthly estimates (Morison et al.,
2012; Mizobata et al., 2016; Armitage et al., 2016; Morison et al., 2018; Rose et al., 2019; Morison et al., 2021; Prandi et al.,
2021). Furthermore, so far only one study by Armitage et al. (2017) has provided and evaluated monthly maps of geostrophic
velocities.

In this study we provide and assess a new Arctic-wide gridded dataset of sea surface height and geostrophic velocity, covering up to latitude of 88°N at monthly resolution, over the period 2011 to 2020. This dataset was obtained from Cryosat-2 observations covering both the ice-covered and ice-free Arctic Ocean. Our specific objectives are:

- to document the methods used to produce the monthly fields of sea surface height and geostrophic velocity;

- to compare monthly sea surface height fields to an independent altimetry dataset, thereby suggesting methodological steps likely to introduce noise or biases in altimetry gridded products at monthly resolution;

- to assess this dataset through comparisons with in-situ data from the Fram Strait and the Laptev Sea continental slope, including multi-year mooring-based current time series.

This paper is structured as follows. In Sect. 2 we describe how altimetry-derived variables are commonly calculated, thereby defining the notation used in this work. In Sect. 3 we provide a description (e.g, sources, spatial and temporal coverage) of: the altimetry data used to derive our monthly dataset; the independent altimetry and in-situ datasets used for evaluation. In the methods section we first describe the in-situ data processing (Sect. 4.1) and then the derivation of monthly gridded sea surface height and geostrophic velocity from altimetry observations (Sect. 4.2, 4.3, 4.4). In Sect. 5 we present the monthly fields and their evaluation against independent altimetry measurements and in-situ data. Comparing against in-situ data we identify the temporal and spatial scales over which they have highest agreement. In the same section we also describe the seasonal cycle emerging from the final monthly maps. Lastly, in Sect. 6 we discuss the spatial and temporal resolution of our dataset and put the emerging features of the seasonal cycle in context with findings from other studies.
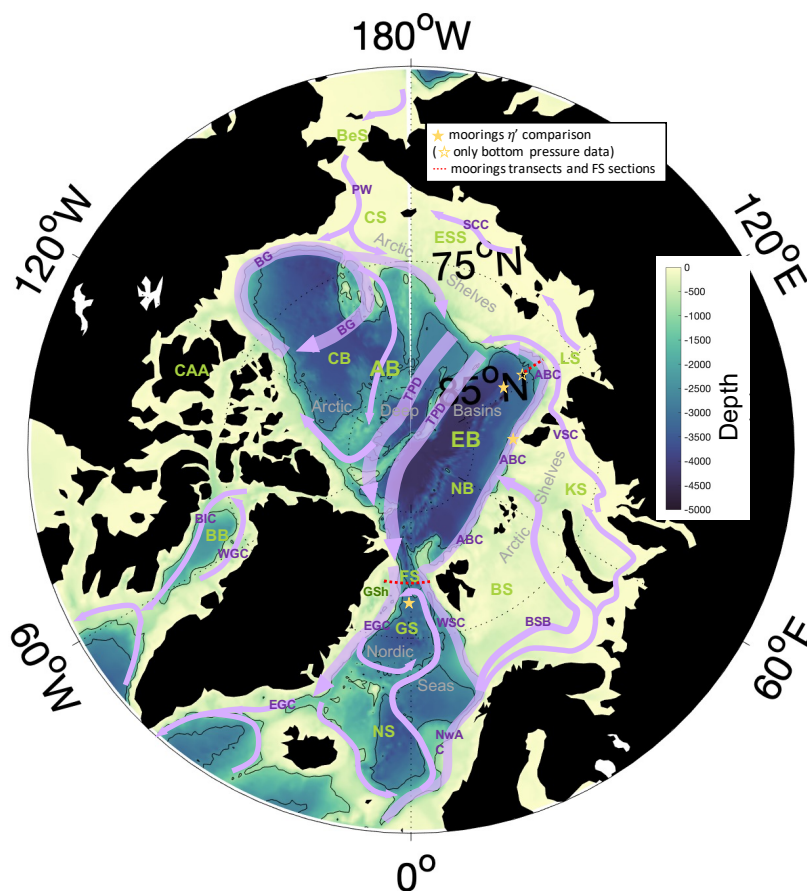
Figure 1. Arctic Ocean map and bathymetry (IBCAO, Jakobsson et al., 2012) with the main sub-regions (green acronyms) and the mean surface circulation pathways (purple arrows and acronyms). Depth contours are drawn at 1000 m and 2000 m depth. **Regions**: Nordic Seas: Greenland Sea (GS), Norwegian Sea (NS); Arctic Shelves: Barents Sea (BS), Kara Sea (KS), Laptev Sea (LS), East Siberian Sea (ESS), Chukchi Sea (CS), Greenland Shelf (GSh); Arctic Deep Basins: Canada Basin (CB), Eurasian Basins (EB), Nansen Basin (NB); Baffin Bay (BB); Canadian Arctic Archipelago (CAA); Fram Strait (FS); Bering Strait (BeS). **Currents**: West Spitsbergen Current (WSC); Norwegian Atlantic Current (NwAC); Barents Sea Branch (BSB); Vilkitsky Strait Current (VSC); Arctic Boundary Current (ABC); Siberian Coastal Current (SCC); Pacific Water inflow (PW); Beaufort Gyre (BG); TransPolar Drift (TPD); East Greenland Current (EGC); West Greenland Current (WGC); Baffin Island Current (BIC).

2 Ocean altimetry background

In oceanography, studying sea level variability is relevant to understand underlying processes linked to steric and mass variations in the water column. These variations can be measured separately by means of in-situ hydrographic profiles (steric) and ocean bottom pressure records (mass), though with limitations in terms of spatial and temporal coverage. An integrated measure of the spatial and temporal variability of these two components, known as dynamic ocean topography (η), can be derived over the global ocean from measurements of sea surface height (h), as obtained from satellite altimetry. In the following, we summarize how η can be derived from altimetry measurements and introduce some notation relevant to satellite altimetry.

h is the ocean height over a reference ellipsoid (e.g, WGS84 for Cryosat-2) and is calculated by subtracting the measurement of the satellite range to the sea surface (R) from the satellite altitude H over the ellipsoid:

$$h = H - (R + C) \tag{1}$$

where C are corrections to the R measurement. η is then derived from h by removing the geoid height (G), i.e. the static ocean height component given the Earth's gravitational field, as follows:

$$\eta(t) = h(t) - G \tag{2}$$

The time varying component of η, the sea surface height anomaly η', is given by h referenced to a long-term mean sea surface height $\langle h \rangle$:

$$\eta'(t) = h'(t) = h(t) - \langle h \rangle \tag{3}$$

In order to compute the absolute geostrophic velocity, η is reconstructed by adding the mean dynamic topography $\langle \eta \rangle$, the temporal mean of η. This is derived from $\langle h \rangle$ by removing G, as estimated via a geoid model (e.g., Rio et al., 2011; Farrell et al., 2012; Knudsen et al., 2019; Mulet et al., 2021).

η is used to derive geostrophic velocities at the sea surface. Geostrophic velocities result from the balance of the pressure gradient force and the Coriolis force, valid in the Arctic on spatial scales larger than few kilometres (Nurser and Bacon, 2014) and time scales longer than a few days. The two components can be expressed as:

$$\begin{cases} u_g = -\frac{g}{f\,R_e}\frac{\partial \eta}{\partial \theta} \\ v_g = \frac{g}{f\,R_e\,cos(\theta)}\frac{\partial \eta}{\partial \phi} \end{cases} \tag{4}$$

where θ and ϕ are latitude and longitude converted to radian angles, R_e is the Earth radius, g is the gravitational acceleration and f is the Coriolis parameter.

The nomenclature introduced in this section will be used below to describe the datasets used and the ones resulting from the present analysis.

3 Data

3.1 Cryosat-2 sea surface height in ice-covered and ice-free regions

The monthly gridded dataset generated in this study is based on two sets of η' observations along the satellite ground track
(projection of its orbit at the ground), one over ice-covered and a second over ice-free areas. Observations are from the European
Space Agency's (ESA) Cryosat-2 mission, provided along the satellite tracks (ESA level L2, Bouzinac, 2012). For ice-covered
areas, down to ice concentration 15%, we use the Alfred Wegener Institute (AWI) dataset (data version 2.4, available at
https://www.meereisportal.de/ Hendricks et al., 2021). This includes year round data (including summer), with along-track
resolution of approximately 300 m. In this dataset, radar echoes from the surface (waveforms) are classified into sea ice and
open water. Then, sea surface elevations from openings in the sea ice cover (i.e. leads) are retrieved using the retracking
algorithm described by Ricker et al. (2014). The processing includes waveforms in the Synthetic Aperture Radar (SAR) and
the interferometric SAR (SARIn) modes (ESA level L1b dataset; see the areas covered by each altimeter mode at http://cryosat.
mssl.ucl.ac.uk/qa/mode.php). Over the open ocean, up to ice concentration 15%, we use data archived in the Radar Altimetry
Database System, with along-track resolution of 7 km (RADS, available at http://rads.tudelft.nl/rads/rads.shtml Scharroo et al.,
2013; Scharroo, Remko, 2018). From both datasets we select observations between 60º N and 88º N over the period 2011-2020.

All η' observations are referenced to the global DTU15MSS mean sea surface (Technical University of Denmark, updated
from the DTU13MSS described in Andersen et al. (2015)), which uses multimission altimeter data including the satellites
Envisat, ICEsat and Cryosat-2. To reconstruct η, we added our final gridded η' to the mean dynamic topography DTU17MDT,
which is the DTU15MSS relative to the OGMOC geoid model (Knudsen et al., 2019).

3.2 Datasets used for comparisons

We use independent satellite and in-situ datasets to evaluate the final monthly fields of altimetry-derived η' and (u_g, v_g). These
datasets are described below and the location of moorings is indicated in Fig.1.

3.2.1 Sea surface height

Monthly η' fields were compared to an independent satellite gridded dataset over the entire Arctic. This dataset is described
by Armitage et al. (2016) and will be hereafter referred to as CPOM DOT (Centre for Polar Observation and Modelling
Dynamic Ocean Topography, available at http://www.cpom.ucl.ac.uk/dynamic_topography). The CPOM DOT is a regional
Arctic dataset spanning the years 2003-2014, derived from sea surface height observations (relying on the satellite missions
Envisat and Cryosat-2) and a geoid model (GOCO3s). Monthly fields are provided on a $0.75° \times 0.25°$ longitude-latitude grid,
up to a latitude of $82°$ N. CPM DOT was compared to the interpolated η' fields at grid points south of 82º N, for the overlap
period between January 2011 and December 2014. Both datasets were referred to their own temporal average over this period.

We further used several sources of in-situ steric height (the height component due to changes in density) plus ocean bottom pressure equivalent height (related to changes in water mass) as ground truth to (i) correct instrumental biases in the along-track η' and (ii) evaluate the spatial and temporal variability of the η' fields.

In a first step we used steric height from hydrographic profiles collected in the Arctic Deep Basins, plus ocean bottom
135   pressure from the Gravity Recovery and Climate Experiment satellite (GRACE), to correct an instrumental offset existing between the along-track AWI and RADS η' observations (Sect. 4.2.1). The hydrographic profiles cover the period 2011-2014 (observations listed in Rabe et al., 2014; extended to 2014 using the sources listed in Solomon et al., 2021; their Table 2). Steric height was computed following Eq. 7. Ocean bottom pressure is included in the GRACE release 6 data as provided by the the Jet Propulsion Laboratory (data are available online at https://podaac.jpl.nasa.gov/dataset/TELLUS_GRAC_L3_JPL_RL06_
140   LND_v03).

This correction was then evaluated by comparing the η' fields to zonal cross-sections of steric height from the Fram Strait plus GRACE data (Sect. 5.2.1). In the western Fram Strait, the Eastern Greenland Current flows in a region of transition from ice-covered to ice-free areas. This comparison was thus appropriate to verify that the offset applied as a correction to the AWI and RADS datasets did not bias the natural sea surface slope induced by this current. The hydrographic sections were taken
145   at 78° 50' N from a ship-based Conductivity-Temperature-Depth (CTD), between late June and early July in 2011 and 2012 (expeditions ARK-XXVI/1 and ARK-XXVII/1 aboard the RV Polarstern; von Appen et al., 2015). Steric height was computed following equation 7 (Sect. 4.2.1).

Finally, we evaluated the temporal variability of the η' fields at three locations by comparing them locally to data from seafloor moorings. The processing of temperature, salinity and ocean bottom pressure data is described in Sect. 4.1. Both in-
150   situ data and altimetry data from each location were referred to the temporal average over the time span covered by mooring data. The moorings were located in the southern Fram Strait ([78.17º N, 0º E], hereafter FS_S), at the shelf break north of Arctic Cape, the headland of Severnaya Zemlya ([82.22º N, 94.85º E], hereafter AC), and down the continental slope north of the Laptev Sea ([78.46º-81.15º N, 125.70º E], moorings M1_4 and M1_6). FS_S was part of a meridional mooring array deployed by the Alfred Wegener Institute (AWI) in the Fram Strait between 2016 and 2018. This mooring was composed
155   of three CTD sensors at depths of 49 m, 231 m, and 729 m. Data from the FS_S mooring are available in von Appen et al. (2019). The AC was one of seven moorings deployed between 2015 and 2018 within the context of the German-Russian project Changing Arctic Transpolar System (CATS). This mooring was composed of six CTD sensors at 50 m, 131 m, 196 m, 293 m, 593 m, and 1448 m. Moorings M1_4 and M1_6 were part of a six mooring array deployed in the Laptev Sea continental slope between 2013 and 2015 within the Nansen and Amundsen Basins Observations System II project (NABOS-II). Steric
160   height and bottom pressure equivalent height were calculated from the moorings M1_6 and M1_4 respectively, given that not all measurements were available from a single mooring. M1_4 was composed of one McLane Moored Profiler measuring between 70 m and 760 m, and three CTD sensors at 26 m, 42 m and 53 m. Hereafter, the combination of data from the two moorings is indicated as as M1_4p6. Data from the M1_4p6 mooring are available from the Arctic Data Center, (Polyakov, 2016, 2019; Polyakov and Rembert, 2019).

Table 1. Names, position and monthly data availability from the mooring line across the Fram Strait. Variable positions indicate the relocation of the moorings in some years. In the third column, values in parenthesis indicate the years of data availability. Data from mooring records longer than 24 months (underlined) were used to compute correlation with altimetry.

Name	Longitude	Latitude	num. months (years)
F1	8°40' E	78°50' N	7 (2015)
F2	8°20' E	78°49'–79°00' N	**42** (2011-2012,2015-2018)
F3	8°00' E	78°50'–79°00' N	**73** (2011-2018)
F4	7°01' E	78°50'–79°00' N	**71** (2011-2018)
F5	5°40'–6°01' E	78°50'–79°00' N	**73** (2011-2018)
F6	4°20'–5°00' E	78°50'–79°00' N	**34** (2015-2018)
F7	4°00'–4°05' E	78°50' N	**38** (2012-2015)
F8	2°45'–2°48' E	78°50' N	**25** (2012-2014)
F15	1°35'–1°36' E	78°50' N	**42** (2011-2014)
F16	0°00'–0°26' E	78°50' N	**70** (2011-2014, 2016-2018)
F9	0°49' W	78°50' N	21 (2011-2012, 2014)
F10	2°03'–1°59' W	78°50' N	**68** (2011-2016)
F11	3°04' W	78°48' N	9 (2011-2012)
F12	4°01'–3°59' W	78°48' N	13 (2011-2012)
F13	5°00' W	78°50' N	20 (2011-2012)
F14	6°30' W	78°49' N	12 (2011-2012)
F17	8°7 ' W	78°50' N	13 (2011-2012)

3.2.2 Velocity

We used measurements of near-surface velocity from two mooring lines to evaluate monthly geostrophic velocity in the Fram Strait and down the continental slope of the Laptev Sea. We compared the (u_g, v_g) component normal to the mooring line, linearly interpolated to the moorings positions (v_n), to monthly averages of the in-situ measured velocities normal to the transects (v_{ni}). The comparison was limited to those mooring locations where more than 24 months of in-situ data were available at the time of manuscript preparation (Tables 1 and 2).

Table 2. Names, position, monthly data availability and depth range over which ADCP data were averaged, for the mooring array along the Laptev Sea continental slope. Variable positions indicate the relocation of the moorings in some years. In the third column, values in parenthesis indicate the years of data availability. Data from all moorings were used to compute correlation with altimetry.

Name	Longitude	Latitude	num. months (years)	Used depth range (m)
M1_1	125°48'–125°50' E	77°04' N	**62** (2013-2018)	30-50
M1_2	125°48' E	77°10' N	**60** (2013-2018)	10-50
M1_3	125°48' E	77°39' N	**61** (2013-2018)	10-50
M1_4	125°54'–125°58' E	78°28' N	**61** (2013-2018)	10-50

The Fram Strait array comprises 17 moorings located along a zonal section at 78°50' N, between the longitudes 9° W and 8° E, maintained since 1997 by the AWI (moorings F1–F10 and F15/F16; Beszczynska-Möller et al., 2012) and the Norwegian Polar Institute (NPI, moorings F11–F14 and F17; de Steur et al., 2009). Velocity measurements were acquired by Acoustic Doppler Current Profilers (ADCP) and Current Meters (CM). We performed the comparison using the time series recorded by
175 the shallower CM (75 m) and by the ADCP bin nominally closer to the CM sensor depth. The measurement depth can vary between 75 m and 200 m if the mooring line is slanted by currents. Mooring positions and the monthly data availability at the time of manuscript preparation are detailed in Table 1. The mooring data are available through PANGAEA (von Appen et al., 2019; von Appen, 2019).

For the Laptev Sea, data were used from four moorings deployed in a meridional transect along the 126° E meridian within
180 the context of the NABOS-II project (moorings M1_1 to M1_4). ADCP velocity measurements were averaged in the upper 50 m. All four moorings provide a record spanning 5 years, between 2013 and 2018 (data are available from the Arctic Data Center, Polyakov, 2016, 2019; Polyakov and Rembert, 2019). Moorings positions and the monthly data availability are detailed in Table 2.

4 Methods

185 In this section we describe the steps followed to derive monthly fields of η' and geostrophic velocity (u_g, v_g) from along-track satellite measurements. Furthermore, we provide details on the processing of in-situ hydrographic data used for comparison.

4.1 Steric height and bottom pressure at moorings FS_S, AC and M1_4p6

Time series of in-situ steric height anomaly (η'_S) and bottom pressure equivalent height anomaly (η'_P) were computed from mooring based measurements of water density and ocean bottom pressure. The relation between η' and the time anomaly of *i)*
190 the vertical density profile $(\rho'(z))$ and *ii)* the ocean bottom pressure (P'_b), is derived by integration of the hydrostatic balance

from the sea surface down to the bottom depth, D:

$$P_b' = \rho_0 g \eta' + g \int_{-D}^{0} \rho'(z) dz \qquad (5)$$

where g is the gravitational acceleration and ρ_0 is a reference ocean water density, set to 1028 kg m^{-3}. Based on this relation, we defined η_S' and η_P' at the mooring sites FS_S, AC and M1_4p6 as:

$$\begin{cases} \eta_S' = -\frac{1}{\rho_0} \int_{-D}^{0} \rho'(z) dz \\ \eta_P' = \frac{P_b'}{\rho_0 g} \end{cases} \qquad (6)$$

Vertical profiles, $\rho'(z)$, were obtained from temperature and salinity profiles using the Fofonoff, N.P, and Millard, R.C. (1983) formula for density. In turn, temperature and salinity profiles were obtained from moored-sensor data by linear interpolation on a regular pressure grid (2 dbar) between the shallowest sensor (FS_S = 50 m, AC = 50 m, M1_4p6 = 26 m) and the deepest sensor (FS_S = 729 m, AC = 1448 m, M1_4p6 = 700 m). Above the shallowest sensor, data were extrapolated to the sea surface, assuming temperature and salinity constant and equal to the uppermost measurement. Below the deepest sensor we assumed the density anomalies to be zero and did not perform extrapolation to the bottom. This conservative approach might have resulted in the underestimation of η_S'. Ocean bottom pressure records P_b' were de-tided using the Matlab function t_tide (Pawlowicz et al., 2002), by performing a tidal analysis on the records and removing the resulting tidal time series. Linear trends were removed to account for instrumental drifts. Unfortunately the time series at FS_S exhibited large pressure anomalies, developing on timescales of several months, whose amplitude was at least one order of magnitude too large to be explained by changes in ocean currents. Therefore, we high-pass filtered this time series with a cutoff frequency of 2 months. All other bottom pressure time series were not affected.

4.2 Along-track sea surface height anomaly

We generated an Arctic-wide dataset of along-track η' by merging the AWI and RADS η' datasets. Inconsistencies between the two datasets were reduced by: i) creating a uniform along-track sampling, ii) reducing biases due to different retracking algorithms, and iii) substituting geophysical corrections where two different corrections were used in the two source products. In this section we first give details about these methods and then present an estimate of the along-track η' observational uncertainty.

4.2.1 Merging leads and open ocean data

Prior to merging the AWI and RADS datasets we standardized their along-track sampling rates, which originally were 300 m and 7 km respectively. With this aim, the AWI dataset was first smoothed by averaging over a 7 km along-track moving window, and then linearly interpolated, following time, onto equally spaced locations (7 km) along the satellite tracks.

A step-like variation in the η' observations at ocean-ice transitions appeared because different models are used to retrack radar signal returns in ice-covered and ice-free regions (Fig. 2a). This is commonly referred to as the "lead-open ocean bias"

220 (Giles et al., 2012). Due to the technical nature of this bias, it is difficult to determine the true bias in the post processing phase. This is why differences between leads and open ocean are usually corrected in terms of a simple offset (e.g., Giles et al., 2012; Armitage et al., 2016; Morison et al., 2018). To estimate the offset, we compared altimetry to independent in-situ hydrography data, similarly to the approach taken by Morison et al. (2018). This approach gives the advantage that circulation features derived from spatial η difference at the transition between AWI and RADS data will be consistent with in-situ hydrography.

225 A good proxy for altimetry-derived η is the sum of hydrography-derived steric height (h_S), and GRACE-derived ocean bottom pressure (h_P, equivalent water thickness). We used hydrographic profiles in the Arctic Deep Basins (Fig. 2b) and compared those to the AWI and RADS along track η (given by $\eta = \eta' + \langle\eta\rangle$, where $\langle\eta\rangle$ is the DTU17MDT described in Knudsen et al., 2019). We computed h_S as the vertical integral of the specific volume anomaly $\delta(p)$ relative to 400 db (Fofonoff, N.P, and Millard, R.C., 1983):

$$230 \quad h_S = g^{-1} \int_0^{400} \delta(p)\, dp \qquad (7)$$

where $\delta(p) = v(S,T,p) - v(35,0,p)$, and $v(S,T,p) = 1/\rho(S,T,p)$. The software used is from the seawater library for Matlab (Mathworks), Version 3.1 (Morgan and Pender, 2009).

η and $h_S + h_P$ were compared using all available data in the overlapping period 2011-2014. All η, h_S and h_P data points were bin-averaged on an equal area grid with a resolution of 25-km. At each bin, average η from AWI and RADS datasets
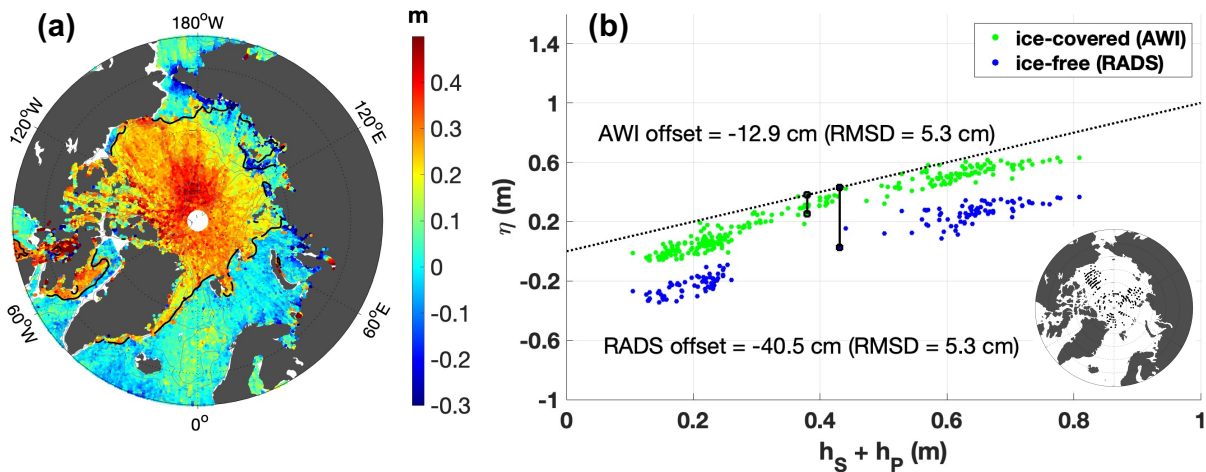
Figure 2. Characterisation of the respective η' bias over leads and open ocean. (a) Scatter plot of AWI (ice-covered) and RADS (ice-free) η' observations for July 2015 prior correcting the offset. The black solid line indicates the 15% sea ice concentration as derived from the OSI SAF ice concentration products (archive OSI-401-b, available at ftp://osisaf.met.no/archive/ice/conc/). (b) steric height plus ocean bottom pressure ($h_S + h_P$) versus η for the ice-covered altimetry data (AWI) and ice-free altimetry data (RADS). Vertical bars indicate the offset between the two altimetry datasets and $h_S + h_P$. Grid points where η and $h_S + h_P$ overlap are indicated in the inset panel.

235 were compared separately to h_S+h_P. In Fig. 2b we show the result of this comparison. Both AWI and RADS data are linearly related to h_S+h_P, with a correlation coefficient of 0.98. This gave us confidence that the AWI and RADS dataset differed by a simple offset, and that altimetry-derived η patterns are consistent with in-situ hydrography. We computed two separate offset values, for the AWI and RADS datasets, by taking the average difference between binned η and binned h_S+h_P in ice-covered and ice-free regions respectively. The two offsets amount to -12.9 cm and -40.0 cm. We corrected altimetry data by removing

240 each offset from the respective along-track η'. After correcting for the two offsets, η and h_S+h_P had a RMSD of 5.3 cm over a range of 70 cm.

4.2.2 Corrections

As second step, we checked that all corrections applied to the satellite range R (Eq. 1) were consistent between ice-covered and ice-free regions (Table 3 lists the products used here). Standard corrections (European Space Agency, 2016) were applied to

245 both regions to account for i) the reduction in satellite signal speed caused by the presence of the atmosphere (dry gases, water vapour, ions); ii) the difference in reflection properties of wave troughs and crests at the sea surface (sea state bias correction, applied solely in the open ocean); and iii) solid earth tides.

Two further corrections are used to remove the high frequency ocean variability due to ocean tides and the ocean response to atmospheric pressure and wind forcing. These corrections contribute to reduce the aliasing of sub-monthly temporal changes

250 into spatial variability, which emerges in average fields as meridionally elongated patterns (meridional "trackiness", Stammer et al., 2000). In order to remove the most variability, we tested two products for each correction. First, to correct ocean tides we used the model FES2014 (Lyard et al., 2021), a more recent version of the FES2004 model (provided by ESA as standard correction product; Lyard et al., 2006). FES2014 was previously found to perform better than FES2004 in the Arctic (Cancet et al., 2018), and has been already used to correct most recent satellite altimetry products in this region (e.g., Rose et al., 2019;

255 Prandi et al., 2021). Furthermore, in support of our choice, we found that the noise on the monthly fields, in areas of high tidal amplitude, was reduced by 20% by using FES2014 with respect to FES2004 (Appendix A).

To correct the effect of atmospheric pressure and wind forcing, we used the Dynamic Atmosphere Correction (DAC, Carrère et al., 2016). The DAC is today conventionally used over the global ocean because it better suppresses the high frequency variability due to non-local forcing (Carrère and Lyard, 2003; Quinn and Ponte, 2012; Carrère et al., 2016). However, for

260 ice-covered regions ESA still suggests using an Inverted Barometer (IB) formula, which only accounts for the ocean response to local pressure forcing. This is because to date there is little knowledge about which of the DAC and IB corrections performs better in ice-covered regions (e.g., Robbins et al., 2016). Studies from the last two decades have shown that the deviation of ocean response from a simple local response is larger at higher latitudes (e.g., Stammer et al., 2000; Vinogradova et al., 2007; Quinn and Ponte, 2012). In the Arctic, the effect of pressure and wind forcing is not only local, but also travels across the

265 region in the form of mass waves (Fukumori et al., 1998; Peralta-Ferriz et al., 2011; Fukumori et al., 2015; Danielson et al., 2020). This indicates that it would be appropriate to apply the DAC to both, ice-covered and ice-free regions.

To support our choice of using DAC over IB, we looked at which of them reduced the standard deviation of the along-track η' the most with respect to the uncorrected η' (see Appendix B). Results showed that DAC outperforms the IB in shallow shelf

Table 3. Altimetry corrections applied in this study. Acronyms: ECMWF (European Centre for Medium-range Weather Forecast); CNES (Centre National d'Etudes Spatiales); MOG2D (Modèle d'ondes de gravité 2D); FES2004 (Finite Element Solution 2004); GDR-E (Geophysical Data Record, version E).

Correction	Source	Reference
Dry troposphere	derived from mean surface pressure, based on the ECMWF model	European Space Agency (2016)
Wet troposphere	derived from mean surface pressure, based on the ECMWF model	European Space Agency (2016)
Ionosphere	Global Ionospheric Map, provided by CNES	Komjathy and Born (1999)
Dynamic Atmosphere	Inverted Barometer + MOG2D barotropic model	Carrère et al. (2016)
Sea State Bias (only open ocean)	Hybrid (mix between parametric and non-parametric techniques)	Scharroo and Lillibridge (2005)
Ocean Tide	FES2014	Lyard et al. (2021)
Solid Earth Tide	Cartwright model	Cartwright and Edden (1973)
Geocentric Polar Tide	Instantaneous Polar Location files (sourced from CNES)	Wahr (1985)
Orbit	GDR-E	European Space Agency (2016)

regions (particularly the East Siberian Sea and the Chukchi Sea) and that they perform equally well over the deep basins (Fig.
270 B1). For instance, in the East Siberian Sea the DAC reduced the uncorrected η' standard deviation by 50% at periods shorter
than 20 days, in contrast to no reduction when applying a simple IB (see Table B1). The improvement of DAC with respect to
IB over the shelves appears also in the η' monthly grids, where meridionally oriented patterns of η' are evidently reduced (Fig.
B2).

4.2.3 Merged along-track dataset and uncertainty estimate

275 The final merged along-track dataset is composed of two sub-datasets, one for the ice-covered region and one for the ice-free
region. The consistency of these two sub-datasets is indicated by their comparable Arctic-wide standard deviation over the
period 2011-2018 (11.1 cm and 10.4 cm, respectively). As an example of the final along track dataset, Fig. 3 shows data from
each week of July 2015. In panel (b) we can see, from an example satellite pass, that η' values transition smoothly along the
track from ice-covered to ice-free areas.

280 We note, though, that there is some residual sub-monthly variability. For instance, Fig. 3a shows a decrease of η' of $\sim$20
cm north of Greenland between the first and the fourth week of July 2015. This shows that, despite correcting high frequency
variability using the DAC and a state of the art ocean tidal correction, η' is subject to residual large scale variability on
time scales shorter than a month. Constructing monthly maps based on sampling this large scale, high frequency variability
at different times in different locations, will artificially produce short wavelength patterns. A clear example of this pattern is
285 shown in Appendix C, highlighting that residual high frequency variability can result in representativeness error on the monthly
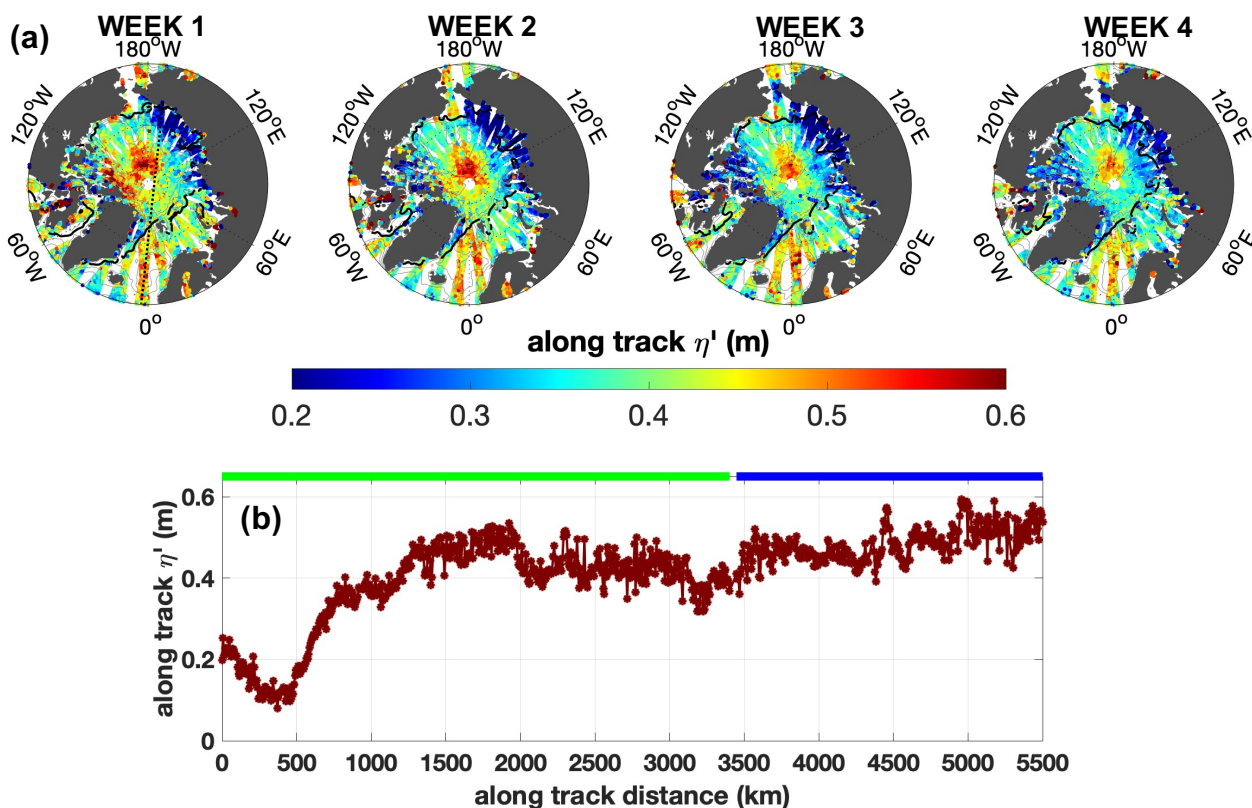
Figure 3. Example of the along-track η' dataset covering the ice-covered and ice-free Arctic Ocean. (a) Weekly availability of along-track data in the month of July 2015. The black solid line indicates the 15% sea ice concentration as derived from the OSI SAF ice concentration products. (b) η' along the satellite track indicated with a dashed black line in panel (a), passing over the Arctic Ocean on the 1st of July 2015, between 19:30 and 20:30 UTC; data in ice-covered areas are marked by a green line and data from the ice-free areas by a blue line. In panel (b), the along-track distance is indicated from Russia towards the Atlantic.

fields. We address this issue in phase of interpolation (Sect. 4.3) and provide in Sect. 4.3.3 an estimate of the contribution of this unresolved variability to the error on the monthly η' fields.

Furthermore, several sources contribute to the observational uncertainty on the along-track η' observations. These are namely the altimeter measurement uncertainty, the waveform retracking method, the corrections and orbit uncertainty. Given the diffi-
290 culty of assessing the contribution of each of these sources, we provide here a comprehensive estimate of the observational uncertainty based on the absolute difference of the along-track η' at satellite tracks crossovers (Fig. 4). We first defined crossovers as those pairs of η' observations within a distance of 7 km. We excluded pairs belonging to the same satellite pass by verifying that they are separated by more than one hour. Considering the large number of data, we organised observations in an equal area grid of about 100 km and computed the absolute value of η' differences at crossovers only within selected cells
295 (dots in the inset of Fig. 4). In Fig. 4 we see that the crossover difference is small for short time differences and increases as
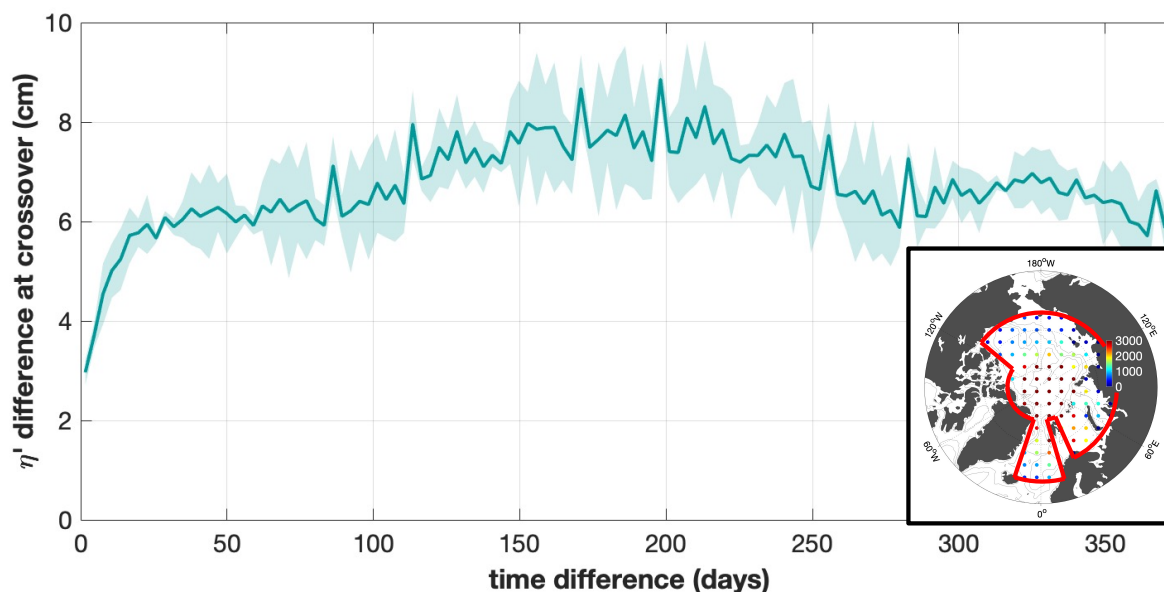
Figure 4. Absolute value of η' difference at crossovers between satellite tracks in a period of time up to 1 year, computed using data inside the red line in the inset panel. The solid line in the main panel is the crossover difference averaged every 3 days; the shaded area shows the standard deviation of crossover difference, averaged every half a day. Crossovers differences were computed using data within 100 km around the locations indicated in the inset panel. The color of dots in the inset panel indicates the number of crossovers found around that location.

crossovers are separated by a larger time difference. For crossovers very close in time, we expect the difference to approximate the observational uncertainty, while we expect it to increase with time due to additional variability. Therefore, we estimated the observational uncertainty as the average difference at crossovers separated by no more than 3 days, which is 3 cm.

This analysis provides additional information about the η' de-correlation time scale. The η' crossover difference increases
300 with time above the uncertainty due to local variability. Fig. 4 shows that variability increases very rapidly by about 3 cm in the first couple of weeks, then by a further 2 cm after six months, to decrease then again by 2 cm after a full seasonal cycle. This indicates that, at time scales shorter than one year, η' has a short de-correlation time scale below one month (in agreement with Landy et al., 2021) and a long de-correlation time scale of six months.

4.3 Gridded sea surface height anomaly

305 We generated monthly η' fields over the period 2011-2020, by interpolation of the along-track data onto a longitude-latitude grid of resolution $0.75° \times 0.25°$, from $60°$ N to $88°$ N. In section 4.3.1 we provide details about the interpolation method used. In Sect. 4.3.2 we explain how, to reduce the noise due to residual sub-monthly variability, we applied the interpolation to weekly subsets of η' observations, which were then averaged to obtain monthly fields. Finally we provide a global estimate of the standard error on the monthly η' fields in Sect. 4.3.3.

4.3.1 Interpolation using the Data-Interpolating Variational Analysis

Along track data were interpolated to obtain η' fields on a regular latitude-longitude grid. We used the Data-Interpolating Variational Analysis (DIVA, Troupin et al., 2012; Barth et al., 2014), a tool based on a technique called variational inverse method (VIM, Brasseur and Haus, 1991). DIVA has been successfully applied in the past by several studies (e.g., Tyberghein et al., 2012; Capet et al., 2014; Lenartz et al., 2017; Iona et al., 2018; Belgacem et al., 2021) to a variety of data types (e.g., temperature, salinity, chlorophyll concentration, nutrients, air pollutants), spatial and temporal extents, and regions (global ocean, Mediterranean Sea, Black Sea). We applied this method for the first time to altimetry observations in the Arctic Ocean.

Rixen et al. (2000) showed that the performance of the VIM is comparable to the widely used optimal interpolation technique (in its original formulation, Bretherton et al., 1976). DIVA offers advantages when treating large datasets in regions of complex topography. One advantage is that the VIM maintains low numerical cost when the number of data points is large compared to the grid points (Rixen et al., 2000). This was suitable for our case, with a number of data points in one month ($\sim 10^5$) ten times larger than the number of grid points ($\sim 10^4$). Furthermore, DIVA allows to naturally decouple basins that are not physically connected by using a regularity constrain based on the gradient and Laplacian of the gridded field (Troupin et al., 2010).

A short description of the working principles of DIVA is given in the following. The optimal field in VIM is found by minimising a cost function (e.g., Brasseur and Haus, 1991; Troupin et al., 2012; Barth et al., 2014, 2021), which satisfies basic requirements for the analysis field φ, such as its closeness to data and its regularity (no abrupt changes). DIVA formalises these principles in a cost function as follows:

$$J(\varphi) = \sum_{i=1}^{N} \mu \left[d_i - \varphi(\mathbf{x}_i) \right]^2 + \int_{\Omega} \frac{1}{L^4}\varphi^2 + \frac{2}{L^2}\nabla\varphi \cdot \nabla\varphi + (\nabla^2\varphi)^2 \, d\Omega \tag{8}$$

In Eq. (8), the first term assures the closeness of the analysis field to the data. This is achieved by globally minimizing the difference between φ at the data locations $\mathbf{x}_i$, and the data themselves d_i, which are associated to a weight μ. The second term generates a smooth field over the domain Ω (Troupin et al., 2012), where L defines the length scale over which the data should be propagated spatially. In general, the field φ and the data d_i should be understood as anomalies relative to a background estimate. The data weights μ are directly proportional to the signal-to-noise ratio λ (ratio of the error variance of the background estimate, σ^2, to the error variance of the observations, ϵ^2) and inversely proportional to the square of the length scale L (Brasseur et al., 1996):

$$\mu = 4\pi \frac{\lambda}{L^2} \tag{9}$$

As explained further below, the interpretation of weights μ in terms of the signal-to-noise ratio allows DIVA to calculate error maps at low computational cost.

The length scale L is a parameter related to the distance over which ocean state variables decorrelate. In the Arctic Ocean, boundary currents can be as narrow as few tens of kilometres (Beszczynska-Möller et al., 2012; Pnyushkov et al., 2015). Even though satellite altimetry provides a tool to investigate the surface expression of these dynamic features, maps of sea surface height in the Arctic are commonly smoothed over hundreds of kilometres (Kwok and Morison, 2016; Pujol et al., 2016;

Armitage et al., 2016; Rose et al., 2019; Prandi et al., 2021). In order to retain the possibility to resolve Arctic boundary currents in our maps of geostrophic currents, we generated monthly maps using a length scale smaller than a hundred kilometers, while relying on a background field derived using a large length scale. Namely, we applied a two-step interpolation as follows. We
345 first computed a background field using all η' observations in the period 2011-2020, interpolated with a large length scale of 300 km. In a second step, we interpolated weekly subsets of the data relative to the background field using a short length scale of 50 km. As explained in Sect. 4.3.2, we finally obtained monthly maps by averaging four weekly fields. The resolution of the final dataset is further discussed in section 6.3.

The signal-to-noise ratio λ is to be interpreted as the ratio between the fraction of data variance that is representative of the
350 final analysis field (in our case a weekly mean) and the fraction that is to be considered noise. The latter might in general include the observational error as well as representativity errors (e.g., instantaneous measurements are not a good representation of a long term mean). One possible way to give an estimate of λ is the generalized cross validation technique (Troupin et al., 2010). However, this technique has led in past studies to an overestimation of λ when applied to non-independent data (Troupin et al., 2010), in particular in applications where averaged fields were created (Troupin et al., 2012; Lauvset et al., 2016; Belgacem
355 et al., 2021). We estimated instead λ from η' observations as follows, and then evaluated our estimate in the context of values used by previous studies. We based our estimate on the approximation that weekly data subsets were not subject to error of representation (see sections 4.2.3 and 4.3.2). For this reason, we considered the observational uncertainty calculated in Sect. 4.2.3 as the dominant source of noise over a period of one week, hence we took ϵ equal to 4.2 cm. Under the same assumption, we estimated the data signal σ^2 as the spatial variance of weekly data subsets over the area where the observational uncertainty
360 was estimated (see inset panel of Fig. 4), averaged in the period 2011-2020 (which yielded σ equal 8.2 cm). The signal-to-noise ratio λ as defined by the ratio of ϵ^2 and σ^2 was therefore 7.5. This estimate lies in the range of values ($\lambda \sim$ 1-10) applied in previous studies to generate averaged fields using DIVA (Troupin et al., 2010, 2012; Tyberghein et al., 2012; Lauvset et al., 2016; Iona et al., 2018; Watelet et al., 2020; Belgacem et al., 2021). Furthermore, we noted that the standard deviation of our analysed η' fields changed by only a small fraction when varying λ in the range of 1-10.

365 Along with the gridded fields, DIVA has the capability to provide associated error maps using several different methods, each having different computational costs. A review of methods is provided by Beckers et al. (2014). Among these, we selected the clever poorman's estimate due to its fast calculation (CPME, Beckers et al., 2014). The CPME speeds calculations by circumventing the extraction of the data covariance matrix, which is never explicitly computed in DIVA. The CPME takes advantage of the fact that the absolute interpolation error scaled by the variance of the background field can be derived with
370 good approximation by applying the DIVA analysis to a vector of unit values (Beckers et al., 2014). We thus generated maps of relative error via the CPME, given as fraction of the variance of the background field. These maps allow the user to assess the data coverage given by the distribution of the data in space, scaled by the length scale L and the signal-to-noise ratio λ.

4.3.2 Minimisation of sub-monthly variability

As explained in Sec. 4.2.3, the residual sub-monthly variability produces marked meridional trackiness if the interpolation is
375 performed on a monthly set of η' observations (see also Appendix C). To further reduce this variability, we performed the

interpolation on weekly data subsets instead. Monthly η' maps were obtained as the average of four weekly maps, and the associated interpolation error was computed as the quadratic sum of four weekly error maps. By comparing Fig. 5a with Fig. 6a one can appreciate how trackiness is reduced in a given month over the entire Arctic. In Fig. 5b we show in detail the η' profile along a latitude circle, as an example of the trackiness reduction obtained thanks to this approach. The field displayed

380   in Fig. 5c shows the contribution of the sub-monthly variability to the error on the monthly η' fields, computed as explained in Sect. 4.3.3.
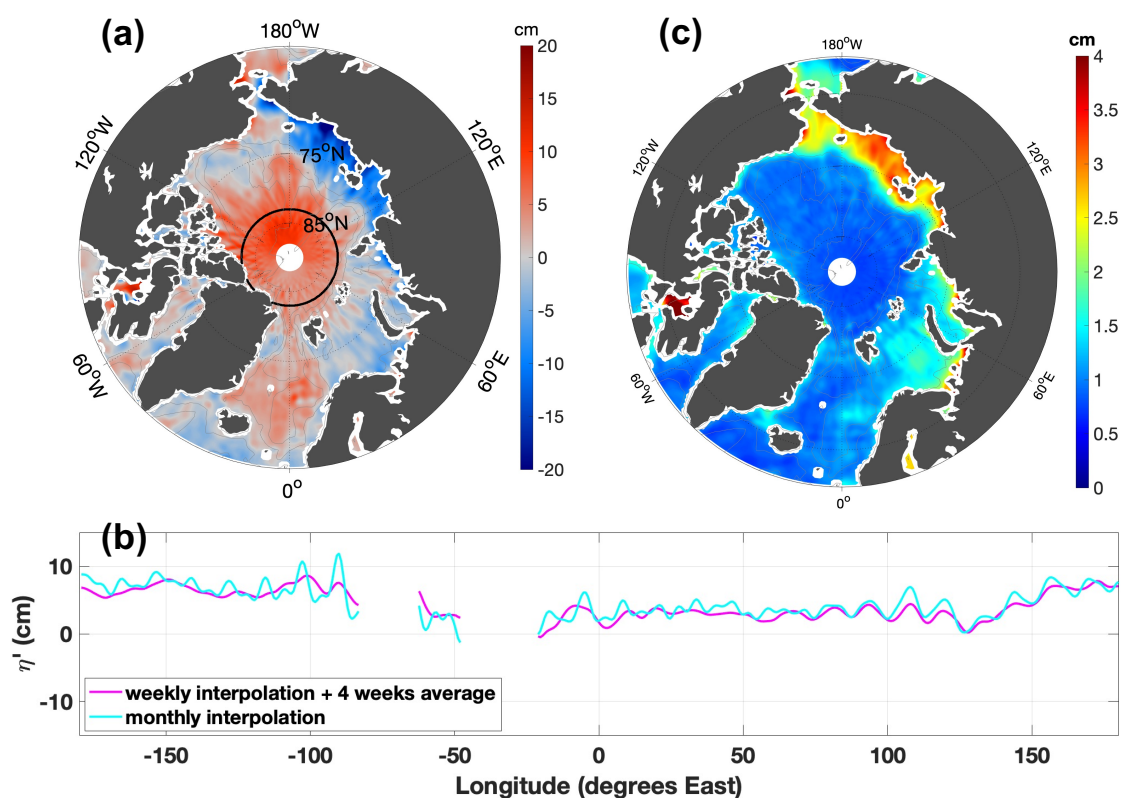
Figure 5. Residual sub-monthly variability in the η' gridded field. (a) The July 2015 monthly gridded η' field obtained by interpolating monthly data input. (b) η' along a latitude (83º N) circle; η' obtained from weekly interpolation plus averaging (Fig. 6a) and from monthly interpolation (panel (a)) are shown with magenta and cyan lines, respectively. (c) The sub-monthly contribution to the standard error on monthly η' maps, computed from weekly maps, averaged over the period 2011-2020. Bathymetry contours are drawn at 100 m, 1000 m and 2500 m depth.

4.3.3 Error on monthly fields

The error in the monthly η' fields comprises a component arising from the observational uncertainty and another arising from representativity error due to unresolved sub-monthly variability. An average estimate of these two contributions to the standard
385 error was computed over the area shown in the inset panel of Fig. 4, as follows.

The component deriving from the observational uncertainty was obtained for each month by dividing our uncertainty estimate of an individual measurement, derived from the crossovers analysis (i.e. 3 cm, Sect. 4.2.3), by the square root of the average number of data points per cell. This component of the standard error, averaged over the period 2011-2020, amounts to 0.9 cm. The monthly component stemming from the sub-monthly variability was first calculated at each grid point as the
390 standard deviation of the four weekly η' values divided by the square root of four. To verify that weekly interpolated fields were statistically independent, we calculated the integral time scale of η' (Emery and Thomson, 2001) from the time series of weekly values between 2011 and 2020, high pass filtered with a cutoff of two months to exclude longer decorrelation time scales. Across the whole Arctic we found an integral time scale of about one week, in agreement with results by Landy et al. (2021), which supported the hypothesis of statistically independent weekly fields. The monthly average standard error yielded
395 by this approach is 1.1 cm over the period 2011-2020. The time average distribution of this contribution is displayed in Fig 5c, which shows values of 1-4 cm in areas shallower than 100 m, with peak values of more than 3 cm in the East Siberian Sea. We assumed that the observational and sub-monthly contributions to the error are independent, and computed the total error by adding them in quadrature. This amounts to 1.4 cm, which is a conservative estimate of the total standard error on monthly averages over the period 2011-2020.

400 ## 4.4 Gridded geostrophic velocity

Monthly η fields were reconstructed by adding up the $\langle\eta\rangle$ DTU17MDT, the η' background field over the period 2011-2020 and the gridded η' maps resulting from the steps described above. Based on the η fields, geostrophic velocity was computed on the output grid following Eq. 4, with partial derivatives approximated by finite differences. The components of velocity on the longitude-latitude grid at indices i, j are given by:

405
$$
\begin{cases}
u_{g,ij} = -\dfrac{g}{f\,R_e}\dfrac{\eta_{i+1,j}-\eta_{i-1,j}}{\theta_{i+1,j}-\theta_{i-1,j}} \\
v_{g,ij} = \dfrac{g}{f\,R_e}\dfrac{1}{cos(\theta_{ij})}\dfrac{\eta_{i+1,j}-\eta_{i-1,j}}{\Phi_{i+1,j}-\Phi_{i-1,j}}
\end{cases}
\tag{10}
$$

where θ and Φ are latitude and longitude converted to radian angles, $f = 2\Omega sin(\theta)$ is the Coriolis parameter (with $\Omega = 7.29 \cdot 10^{-5}$ s^{-1}) and R_e is the Earth radius.

5 Results

Here we first describe the characteristics of the monthly maps of η' and geostrophic velocity (u_g, v_g), then present the results
410 of their comparison with independent datasets, and lastly display the most prominent aspects of the η' and (u_g, v_g) seasonal cycle.
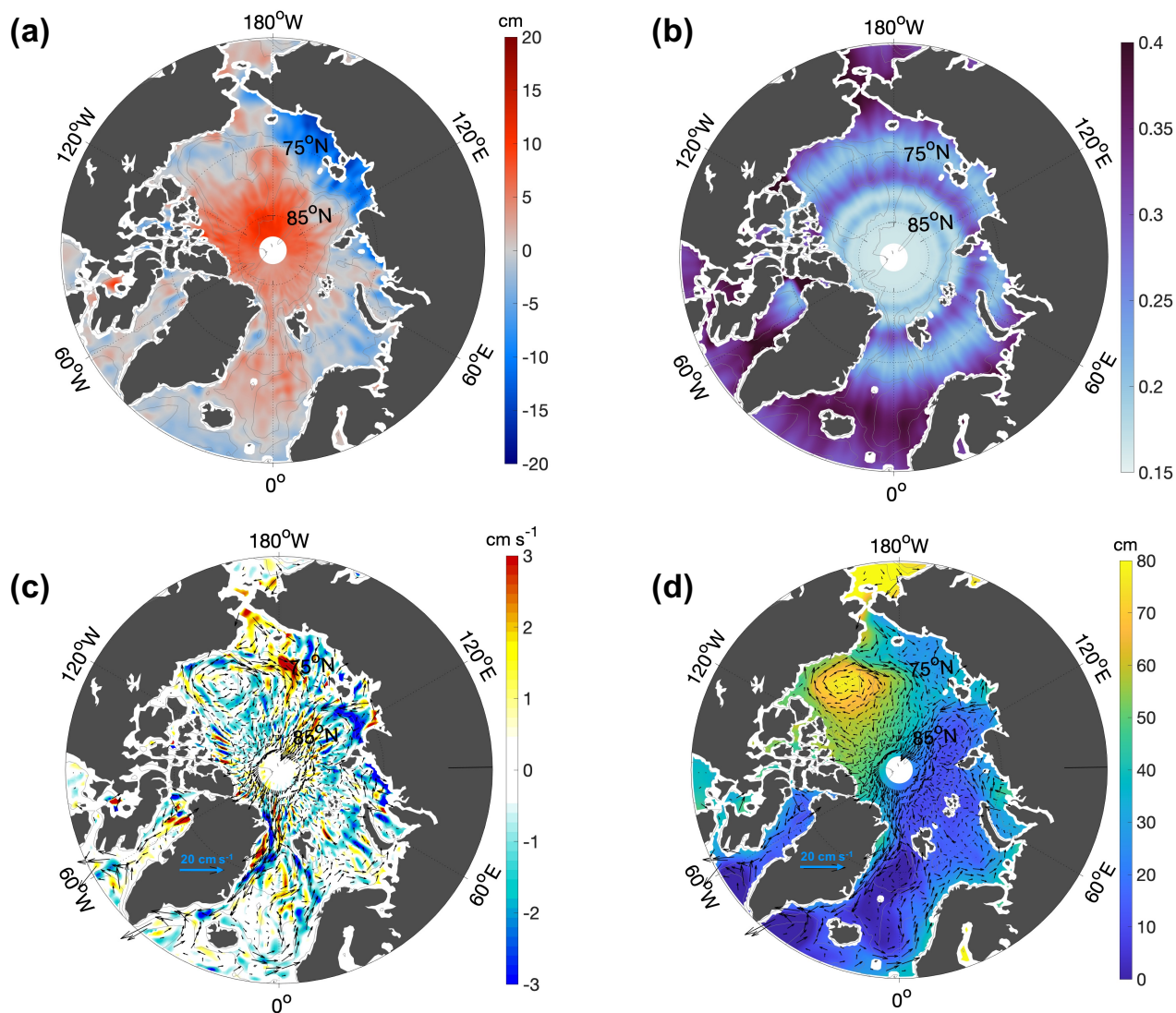
Figure 6. Example of monthly gridded fields included in the final data product, for the month of July 2015. (a) η' field above the 2011-2020 background field. (b) Relative error field on the interpolated η', given as fraction of the variance of the background field. (c) (u_g, v_g) field. Arrows in (c) represent the absolute (u_g, v_g) field for the month of July 2015, whereas colour highlights the anomaly of the monthly geostrophic speed ($V_g = \sqrt{u_g^2 + v_g^2}$) with respect to the the mean geostrophic speed over the period 2011-2020. (d) Dynamic ocean topography (η, background color) and the associated geostrophic velocity field (as in (c)). Bathymetry contours are drawn at 100 m, 1000 m and 2500 m depth.

5.1 Monthly fields of sea surface height anomaly and geostrophic velocity

As an example to describe general characteristics of a given monthly map over the 2011-2020 period, here we present results from the month of July 2015. Fig. 6 shows fields of η', relative error (associated with the interpolation) and (u_g, v_g) for July 2015. The description below makes reference to the Arctic Ocean sub-regions and surface circulation pathways presented in Fig. 1.

In the η' monthly fields we generally find that there are extended regions of either positive or negative values. In Fig. 6a, for instance, η' is positive in the deep regions, i.e. in the Nordic Seas and across the Arctic Deep Basins, and negative over the shelf seas. η' also varies within these regions, being for instance maximum ($\sim$10 cm) north of 85º N, and minimum in the East Siberian Sea. Superimposed on these large scale patterns, residual meridional trackiness appears south of 80° N, especially in shallow areas, where the error related to the residual sub-monthly variability is highest (Fig. 5c).

The relative error for the month of July 2015 is on average 0.23, with a minimum below 0.2 around the North Pole and a maximum above 0.3 south of 70° N (Fig. 6b). The largest relative error values are found in regions with data gaps (see weekly data distribution in Fig. 3a): i) south of 75° N, where the distance between the satellite tracks increases considerably; ii) in a zonal band around 80° N, where the weekly data distribution is not uniform due to the satellite orbit geometry; and iii) in regions covered by multiyear ice during winter months (not shown).

In Fig. 6c we present the geostrophic velocity field (u_g, v_g), with background colors highlighting monthly speed anomalies relative to the 2011-2020 mean speed. The distribution of anomalies aligns well with known circulation pathways, such as those found along steep bottom topography gradients or large scale current patterns like the Beaufort Gyre and the Transpolar Drift. Speed anomalies in July 2015 show that currents are weak around the Nordic Seas (East Greenland Current, West Spitsbergen Current and the Norwegian Atlantic Current) and at the Laptev Sea continental slope (Arctic Boundary Current), while they are intensified in the westernmost branch of the Beaufort Gyre and in the Pacific Water inflow across the Bering Strait. This indicates that our data set yields realistic variability over a large span of the Arctic Ocean. Still, there are small areas where speed anomalies appear along meridionally elongated stripes, i.e., not following bottom topography contours. These patterns result from gradients between residual η' sub-monthly variability and do not correspond to real monthly velocity anomaly.

5.2 Comparison to independent datasets

We evaluated both η' and (u_g, v_g) fields against independent data in order to: i) test the robustness of the monthly η' fields, both in ice-free and ice-covered regions, by comparison to the satellite-derived, gridded CPOM dataset; ii) verify the spatial consistency of our η' fields in the Fram Strait, a region of transition between ice-covered and ice-free ocean; iii) assess the agreement in time and space between our gridded η' and (u_g, v_g) fields and mooring-based data in seasonally ice covered regions over a time span of few years.

5.2.1 Sea surface height

We first tested the robustness of the temporal variability of our monthly η' fields over the entire Arctic. Past studies providing gridded altimetry fields in this region either did not compare to independent altimetry products (Armitage et al., 2016; Kwok and Morison, 2016; Rose et al., 2019), or compared to products that were not tailored for ice covered regions (Prandi et al., 2021). Results from the comparison of our gridded η' fields with the CPOM DOT show good agreement over most of the Arctic domain, with a correlation between datasets above 0.7 for 85% of the grid points (Fig. 7a). The comparison yields lower correlation values (0.3 to 0.7) along the Canadian and Greenland coasts (where the multi year ice persists for most of the year) and in sparse areas of the central Arctic and in the Barents Sea. Only in less than 1% of the domain the correlation is below 0.3 (Baffin Bay). The root-mean-square-deviation (RMSD, Fig. 7b) exhibits low values (2 cm to 4 cm) over more than 80% of the domain, including most of the regions with water depth greater than 100 m. The RMSD is high (7-8 cm) over the East Siberian Sea and Chukchi Sea, where the error due to sub-monthly variability is also highest. These results seem to indicate that altimetry-derived month to month variability is generally robust in relation to the methodology applied, also in ice covered regions, with few exceptions that we will discuss in Sect. 6.
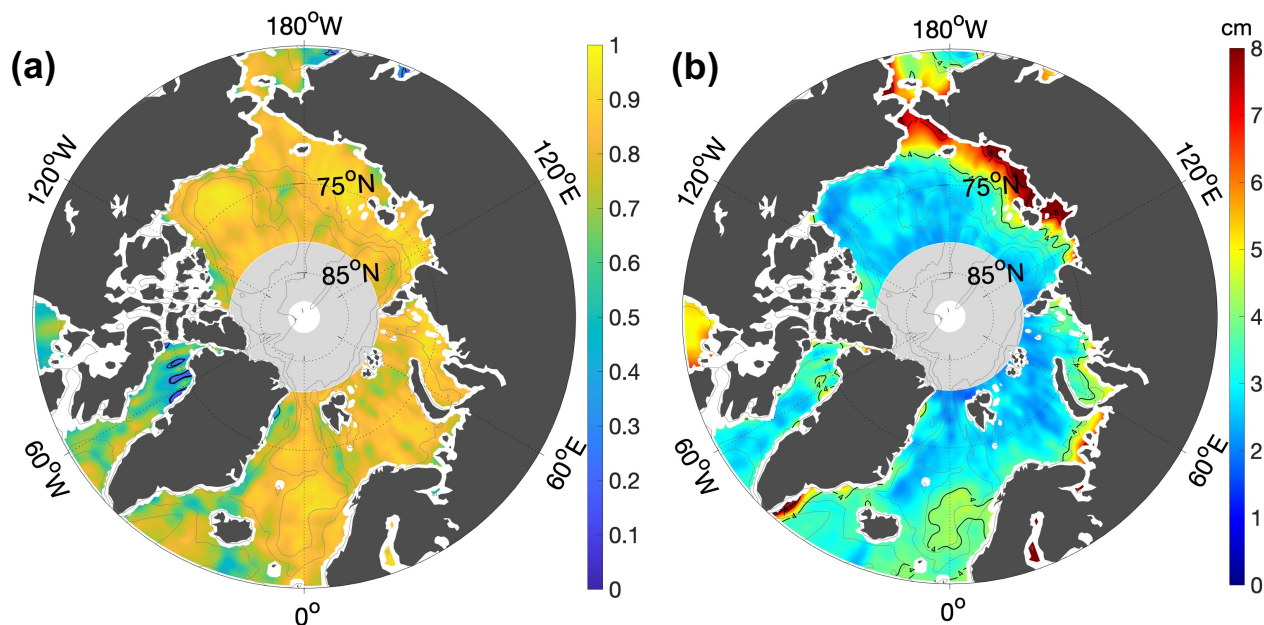
Figure 7. (a) Pearson's correlation coefficient and (b) RMSD between the gridded η' fields as derived in this work and the CPOM DOT published by Armitage et al. (2016). Each dataset was referred to its own average over the period 2011-2014 before comparison. In panel (a), correlation is <0.3 and p-value >0.05 in the small area in the Baffin Bay encircled by a thick black line. In panel (b), thick black lines are contours of 4 cm, 7 cm and 8 cm. The area shaded in gray north of 82° N is not included in the comparison because not covered by the CPOM DOT. Bathymetry contours (dotted lines) are drawn at 100 m, 1000 m and 2500 m depth.
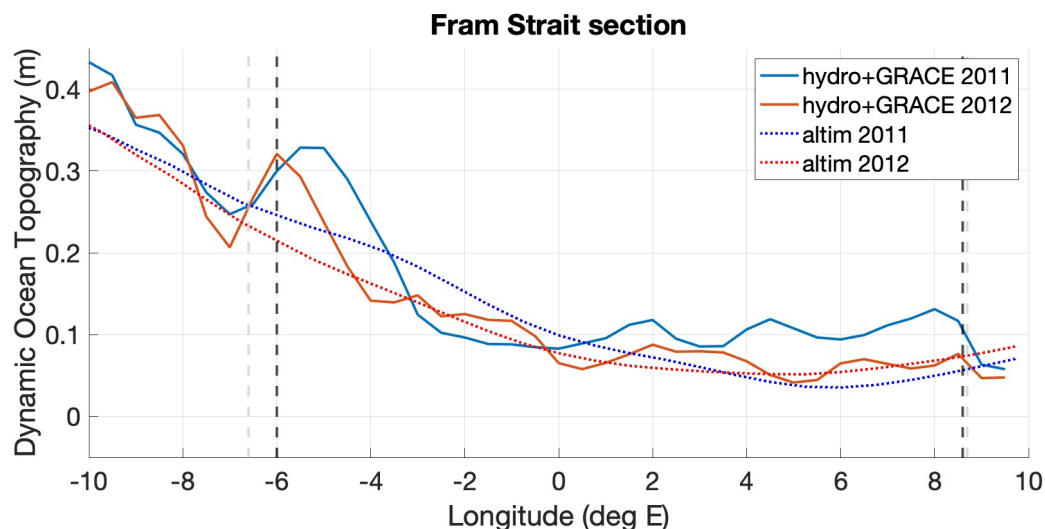
Figure 8. Cross sections of η across the Fram Strait at 79° 50' N in June 2011 and June 2012. Altimetry-derived η is displayed against steric height h_S from in-situ hydrographic sections plus ocean bottom pressure h_P from GRACE. Light gray and dark grey vertical dashed lines indicate the 300 m and 400 m isobaths respectively.

455 Secondly, we wanted to demonstrate that in Fram Strait, a transition zone between ice-covered areas in the west and ice-free areas in the east, the spatial sea surface slope associated with the local ocean circulation is retained in our η fields (computed as described in Sect. 4.4). In order to do this, we carried out a comparison with independent hydrography data, not used for the offset correction displayed in Fig. 2. In Fig. 8 we display two cross sections of altimetry-derived η across the Fram Strait, in the months of June 2011 and June 2012, against dynamic height from ship-based CTD sections plus ocean bottom pressure

460 from GRACE data. In the East Greenland Current (7° W to 2° W), at the transition between ice-covered and ice-free regions in western Fram Strait, the broad cross shelf variation in η is comparable to in-situ data. We note though that the strong local gradients between 7°W and 4°W, each spanning a distance of about 30-40 km, are not captured. This is likely due, on the one hand, to the large length scale used to smooth altimetry data, and on the other hand, to the fact that altimetry profiles represent a monthly average while in-situ data a snapshot of hydrography over the course of a few days. Despite the above mentioned

465 differences, this comparison seems to indicate that the differential offset correction applied to altimetry data between ice free and ice covered areas (shown in Fig. 2) have preserved the broad spatial sea surface slope associated with the East Greenland Current.

After having demonstrated the spatial consistency of our data set, we now turn to the question to which degree the time variability in the gridded η' fields is representative of independently observed variability. For this reason we used mooring time

470 series at different locations in the Arctic Ocean and compared them to time series extracted locally from our η' fields. Time series of η' from altimetry, and $\eta'_P + \eta'_S$ from mooring data (computed as described in Sect. 4.1), are shown in Fig. 9. The correlation between the altimetry and mooring time series is higher than 0.4 and significant (p-value < 0.05) at all three sites.

The correlation is highest at the M1_4p6 mooring, where in-situ hydrography is measured up to 26 m below the sea surface. Sea surface height from altimetry and mooring follow roughly a similar pattern, varying within a range of ±10 cm over the

475 comparison period at all three sites. At the FS_S and the M1_4p6 moorings there are hints of a seasonal oscillation: the signal at FS_S is decreasing from October 2016 to March-April 2017 and then increasing until October 2017, whereas at M1_4p6 η' decreaases during winter and increases again in summer in both years (Fig. 9). At the AC and M1_4p6 moorings, short term variability appears in phase at times, for instance between December 2016 and May 2017 in the former, and between July 2014 and February 2015 in the latter (Fig. 9). There are however, large differences in some months, which is reflected in the RMSD

480 and the η' standard deviation.
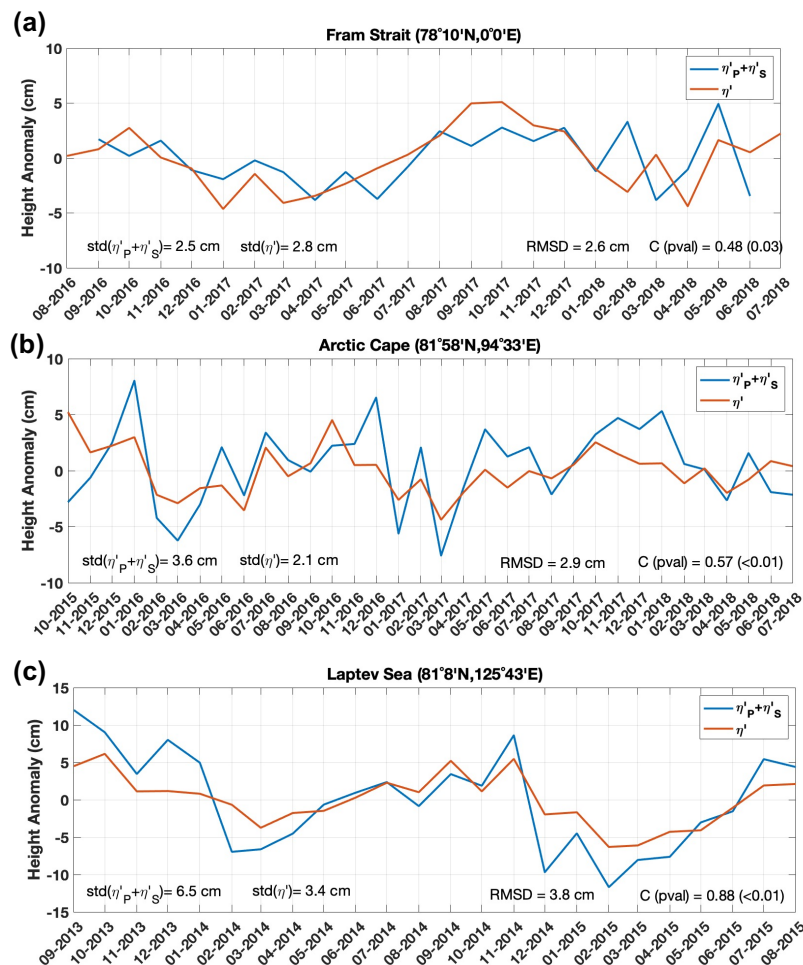
Figure 9. The sea level anomaly ($\eta'_P + \eta'_S$) derived from data at moorings (a) FS_S, (b) AC, (c) M1_4p6 (blue line) is displayed against the η' interpolated at the mooring location (red line). Standard deviations of η' and $\eta'_P + \eta'_S$ are displayed in the bottom left corner, while RMSD and correlation coefficient in the bottom right corner (Pearson's correlation coefficient, where p-value was computed using the effective number of degrees of freedom, Emery and Thomson, 2001).

Table 4. Comparison of altimetry (v_n) and in-situ (v_{ni}) velocities normal to the mooring lines. Moorings are listed, from left to right, respectively as the westernmost to easternmost in the Fram strait and southernmost to northernmost in the Laptev Sea continental slope. The first two rows the Pearson's correlation coefficient and the RMSD between v_n and v_{ni}; correlations with p-value<0.05 are highlighted in bold (p-values were computed using the effective number of degrees of freedom, Emery and Thomson, 2001). The next four rows show the mean and standard deviation of the altimetry-derived v_n and mooring v_{ni} velocities.

	Fram	**Strait**									**Laptev**	**Sea**		
	F10	F16	F15	F8	F7	F6	F5	F4	F3	F2	M1_1	M1_2	M1_3	M1_4
Correlation	0.01	**0.22**	0.17	-0.28	-0.18	0.16	**0.33**	**0.38**	**0.54**	0.30	**0.77**	0.06	0.17	**0.45**
RMSD (cm s^{-1})	5.3	6.8	6.7	5.8	7.2	6.8	6.3	6.7	6.8	7.2	5.7	4.6	2.0	1.1
mean v_n (cm s^{-1})	-7.3	-4.3	-2.9	-1.8	-0.3	0.9	2.8	4.0	4.5	4.5	4.7	4.6	4.1	2.9
mean v_{ni} (cm s^{-1})	-7.9	1.1	-0.8	6.1	-2.5	-2.6	5.3	6.0	17.0	18.1	12.1	3.5	3.4	1.6
std v_n (cm s^{-1})	1.8	1.5	1.3	1.2	1.3	1.3	1.7	1.8	1.7	1.8	2.3	2.2	1.3	0.8
std v_{ni} (cm s^{-1})	5.0	7.1	6.9	5.5	6.9	7.0	6.7	7.2	7.6	7.6	7.4	4.2	1.8	1.2

5.2.2 Velocity

Satellite-derived maps of surface geostrophic velocity offer the advantage of a quasi-synoptic view of ocean surface currents and their variability. However, for several reasons (e.g., sampling pattern, nature of the data) the variability observed from satellite is not the same as the one observed in situ. In our comparison of (u_g, v_g) fields to mooring near-surface velocity, we

485 assessed the spatial and temporal scales over which these two data sources provide consistent information on the underlying variability.

a. Correlation and RMSD at mooring locations

The agreement of altimetry-derived and in-situ velocities at mooring locations is summarized in Table 4. The table presents

490 correlation and RMSD of the velocity component normal to the mooring lines (v_n and v_{ni} respectively), together with their mean and standard deviation at each mooring. Hovmoeller diagrams of velocity normal to the Fram Strait and Laptev Sea mooring lines are displayed in Fig. 10 and 11. In the Fram Strait, the correlation is significant (p-value < 0.05) and higher than 0.3 at moorings F3 to F5, across the continental slope in the eastern part of the strait. At these 3 moorings, both the mean v_n and v_{ni} are consistently positive and comparable or higher than the corresponding standard deviation. The correlation is highest

495 at mooring F3, the mooring with the longest continuous time series. Over the Laptev Sea continental slope the correlation is highest at the M1_1 mooring, in the uppermost part of the slope. At this mooring, v_{ni} is on average four time larger than further down the slope. At the moorings located down the slope, the correlation is lower, being still significant at mooring M1_4, but

non-significant at moorings M1_2 and M1_3.

 b. Spatial and temporal resolution

By examining the mean and standard deviation of velocity along the mooring lines, we note differences between gridded altimetry and in-situ data in terms of spatial and temporal resolution. The mean v_n shows low spatial variability and smooth transitions between nearby sites. Note that this variability is governed by the averaging scales underlying the DTU17MDT product. The scales captured by the DTU17MDT are defined by the resolution of the geoid model used to compute it. Previous studies, mentioning also the geoid model used by DTU17MDT, indicate that these scales are not smaller than 100 km (Gruber and Willberg, 2019; Bruinsma et al., 2014; Farrell et al., 2012). These large scales contrast with the high spatial variability of the v_{ni} mean flow, which is derived by pointwise measurements. This is shown for instance by abrupt changes between moorings F15 and F7 (50 km apart) or between M1_1 and M1_2 (11 km apart). The high spatial variability observed by the mooring data is ascribable to the small Arctic first baroclinic Rossby radius, which is below 10 km in the two study regions (Nurser and Bacon, 2014; von Appen et al., 2016; Pnyushkov et al., 2015). Furthermore, in the altimetry dataset the time variability associated to mesoscale processes is smoothed out due to the 50 km decorrelation scale applied through the interpolation. This is reflected in the v_n standard deviation, which is about four to five times smaller than that of v_{ni} at most moorings.

Table 5. Comparison of spatially averaged altimetry and in-situ velocities. The first two rows show the Pearson's correlation coefficient and RMSD between horizontally averaged v_n and v_{ni}. Each test (described in Sect. 5.2.2b) corresponds to the averaging of data from two or more moorings (names of moorings used in each test and cross-flow distance covered by them are indicated in the header). The last two rows show correlations at frequencies lower and higher than 4 months. All correlations in this table have a p-value <0.01, computed using the effective number of degrees of freedom (Emery and Thomson, 2001).

	test 1	test 2	test 3	test 4	test 5
	20 km	45 km	85 km	11 km	61 km
	F3, F4	F3 to F5	F3 to F7	M1_1, M1_2	M1_1 to M1_3
Correlation	0.55	0.62	0.49	0.61	0.36
RMSD (cm s^{-1})	4.9	3.1	2.6	4.0	2.3
Correlation 4 months low-pass	0.63	0.68	0.61	0.62	0.37
Correlation 4 months high-pass	0.37	0.33	0.11	0.58	0.27

To establish spatial scales over which altimetry-derived currents approximate best the in-situ measured currents, we compared spatially averaged v_n and v_{ni}. We performed five tests, averaging data over sets of at least two moorings chosen among those closest to the shelf break (tests 1 to 5 in Table 5). In order to take in account the fact that time series of moorings closer to each other are less independent, we performed a weighted average of the v_n and v_{ni} time series, by assigning to each mooring

a weight proportional to its distance to the two neighbouring moorings (e.g., for mooring j: $w_j = \frac{d_{j,j-1}+d_{j,j+1}}{2}$, where d is the distance).

In the Fram Strait, averaging over moorings F3 to F5 (test 2, spanning a distance of 45 km) yielded a correlation higher than
520   that using data only from the F3 mooring (where the pointwise comparison was highest, compare Tables 4 and 5). Results from
tests 1 and 3 yielded correlations comparable to that at F3. All three tests reduced the RMSD by about 2-3 cm with respect to
that at F3. At the Laptev Sea continental slope, neither test 4 nor test 5 improved the correlation with respect to the comparison
at the M1_1 mooring. Both tests though reduced the RMSD with respect to the one at M1_1 (2-4 cm lower).

Finally, we looked at the correlation between the spatially averaged v_n and v_{ni} in two frequency bands (Table 5), namely
525   seasonal to interannual (lower than 4 months) and the intra-annual (higher than 4 months) and determined which time scales
are dominant in each dataset. In the seasonal to interannual frequency band, v_n and in v_{ni} correlate better or equally than
without filtering (Table 5), whereas in the intra-seasonal frequency band the correlation worsens. The percentage of variance
explained by each frequency band in each dataset was evaluated as:

$$E = 100\,(1 - \frac{\mathrm{var}(x - x_F)}{\mathrm{var}(x)}) \qquad\qquad (11)$$

530   where x is the horizontally averaged v_n or v_{ni} time series (tests 1 to 5), and x_F is the correspondent filtered time series. We
find that, in all tests, seasonal to interannual frequencies explain most of the variability both in v_n and in v_{ni}. They constitute
about 80% of the total variability in the Fram Strait, and about 90% at the Laptev Sea continental slope.

In Fig. 10a and 11a we can see that the seasonal to interannual frequencies are dominated by seasonal oscillations, which
have similar characteristics in the altimetry and mooring data. The seasonal cycles of v_n and v_{ni} are in phase, with peaks
535   occurring in winter, and troughs in early summer, both in the Fram Strait and at the Laptev Sea continental slope. Furthermore,
v_n and v_{ni} show similarities in the interannual variability. For instance, in the Fram Strait both datasets feature a double peaked
seasonal oscillation in some years (e.g. winters 2013-2014, 2017-2018). At the Laptev Sea continental slope the seasonal cycle
amplitude decreases in both datasets between 2016 and 2018 .
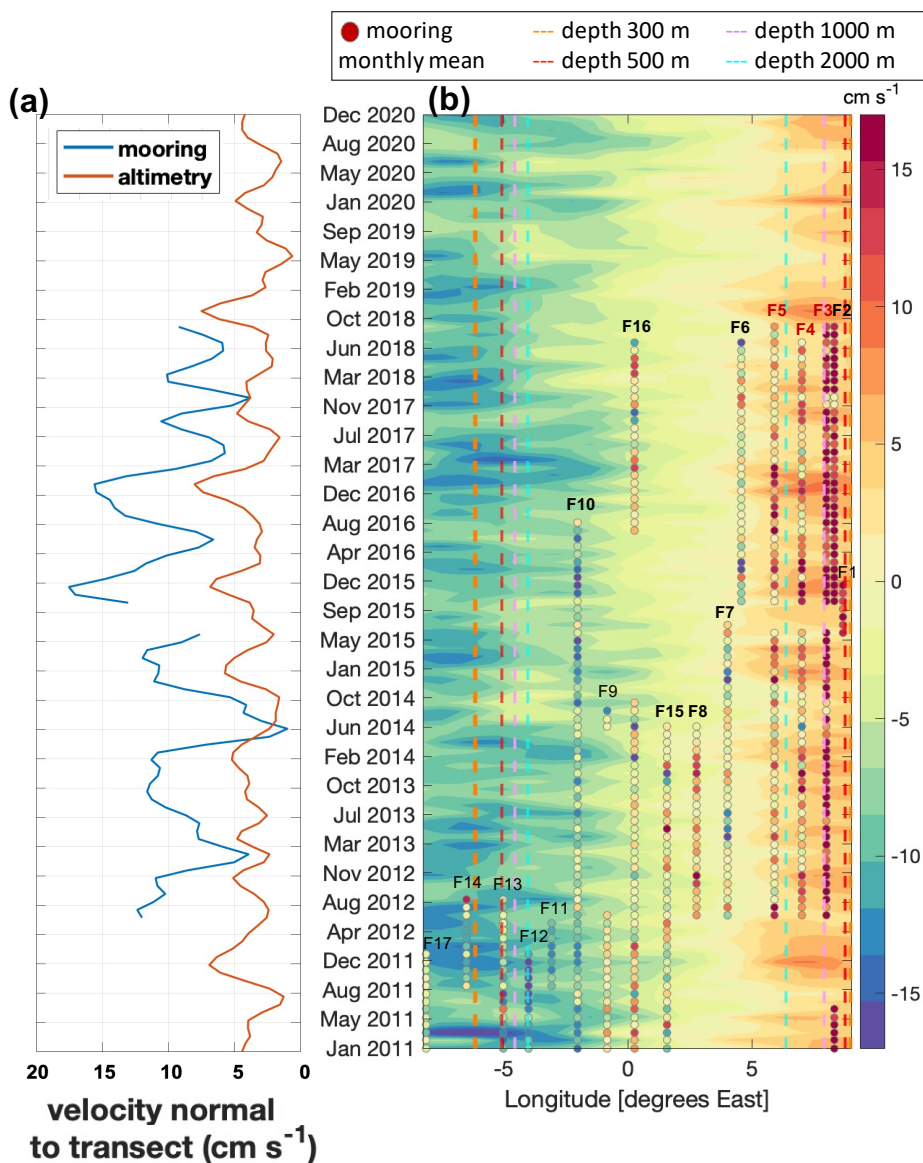
Figure 10. The altimetry-derived geostrophic velocity is shown against the in-situ surface velocity at the moorings transects in the Fram Strait, along latitude 78° 50' N (see Fig. 1). The component of the velocity normal to the transect is evaluated, and positive values represent northward velocity. (a) Longitudinal average of altimetry and in-situ velocity across moorings indicated with red letters in panel (b) (corresponding to test 2, see Sect. 5.2.2); both time series have been filtered with a 4-months low pass filter. (b) Hovmöller diagram representing the monthly temporal evolution of the altimetry-derived cross-transect geostrophic velocity. The circles represent monthly mean values of in-situ cross-transect velocity. On the top part of the diagram we indicated the position of each mooring; at moorings with bold letters, data covered a period longer than 24 months.
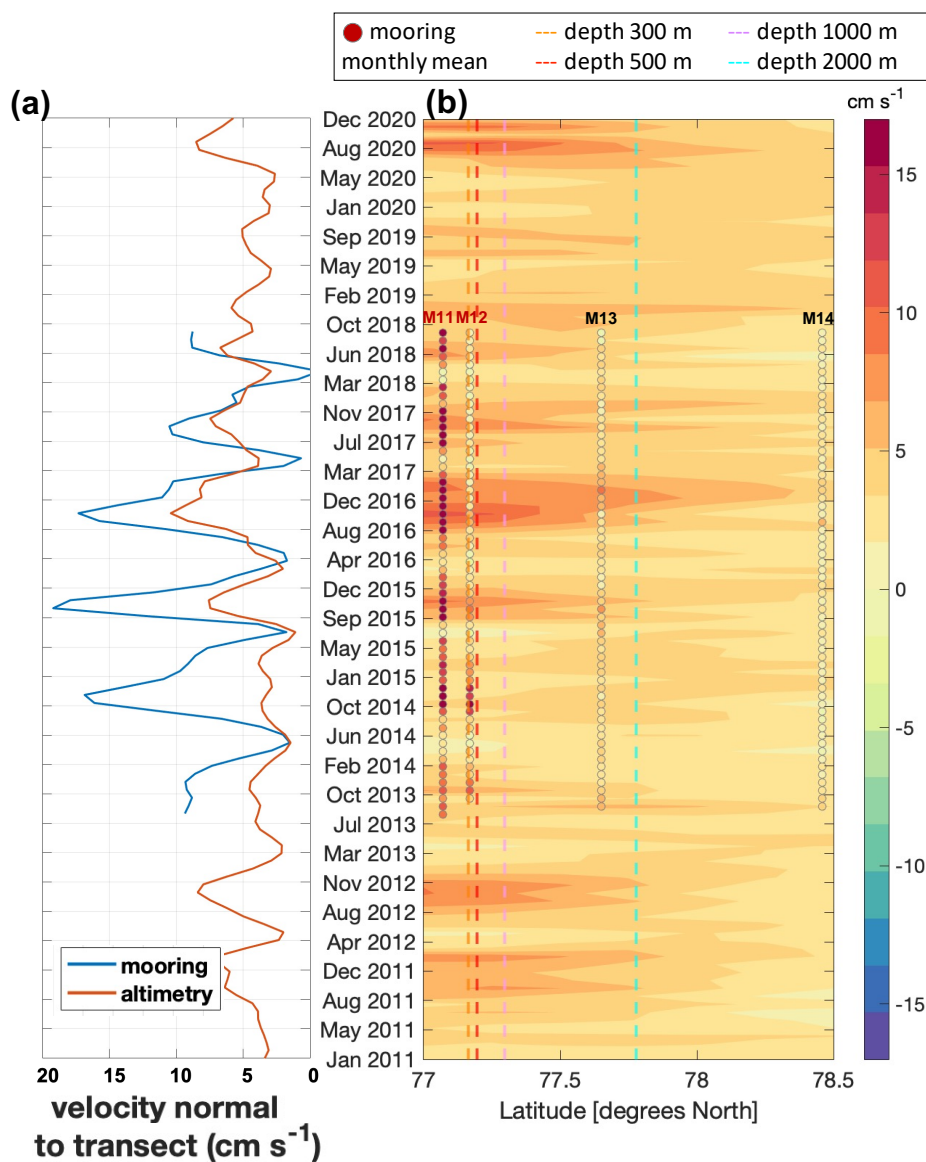
Figure 11. As in Fig. 10, for velocities at the Laptev Sea continental slope, along longitude 126° 50' E (see Fig. 1). The component of the velocity normal to the transect is positive eastward. The time series in panel (a) correspond to test 4 (see text).

5.3 Seasonal cycle

540 The seasonality of the Arctic sea level and surface currents has been studied in several previous works (e.g., Volkov et al., 2013; Armitage et al., 2016; Beszczynska-Möller et al., 2012; Baumann et al., 2018), giving us the opportunity to assess our dataset based on this literature. We defined the seasonal cycle of η', following Volkov et al. (2013), as the harmonic least-square fit to η' with period of one year:

$$\eta'_{seas} = A \cos\left[2\pi\left(\frac{t-\alpha}{P}\right)\right] \tag{12}$$

545 where t is time, $P = 12$ months is the oscillation period, A is the amplitude of the η' seasonal cycle and α its phase (i.e., month when the maximum occurs). We evaluated the fraction of variance explained by η'_{seas} at each grid point following Eq. 11, with η' as x and η'_{seas} as x_F.

In the following text we give an overview of the seasonal cycle observed in η' and (u_g, v_g), with emphasis on the regions where it explains a high fraction of the total variability.

5.3.1 Sea surface height

550

The amplitude A and the phase α of the η' seasonal cycle are shown in Fig. 12. The amplitude ranges between 1 and 8 cm, with values above 3 cm in shallow shelf regions, in the southwestern Canada Basin and in the Nordic Seas (Fig. 12a). In these regions and in the Eurasian Basin, the seasonal cycle explains more than 20% of the total variability. η'_{seas} is maximum in early winter across the Arctic Ocean, even though not uniformly (Fig. 12b). On the Eurasian side, we see a clear divide between 555 shallow and deep regions, with η'_{seas} peaking earliest (September-October) in the Nordic Seas and the Eurasian Basin, and later (November-December) all along the Eurasian shelves, from the Barents Sea to the East Siberian Sea. On the Amerasian side, η'_{seas} peaks earliest in the southwestern Canada Basin and later in the Chukchi Shelf.

In Fig. 12c we also display the monthly climatology of η' observed in selected regions, computed as the January to December monthly averages over the years 2011-2020. We see that the harmonic fit is a good approximation of the climatology in most of 560 these regions. One exception is the secondary peak in June-July exhibited by the climatology in the Canada Basin, the Eurasian Basin, the Laptev and East Siberian Sea, and the northeastern Greenland Shelf.

5.3.2 Geostrophic velocity

Fig. 13 shows the winter (January to March) and summer (June to August) average fields of (u_g, v_g) over the period 2011-2020. Seasonal speed anomalies are most pronounced south of 80ºN, namely along the shelf edges, in some coastal regions, in the 565 southern Canada Basin and in the Barents Sea. The strongest variation in current speed between summer and winter is about 3 cm s^{-1}. The time of seasonal maximum of some of the main Arctic currents is shown in Table 6. From the comparison between summer and winter current anomalies we observe a basin wide, coherent seasonal acceleration of the Arctic slope currents in winter and a deceleration in summer. The speed of these slope currents peaks between September and April. Namely, currents along the Nansen Basin shelf break, between the Fram Strait and the Lomonosov Ridge, peak in early winter (September

570 to December); currents along the eastern shelf break of the Nordic Seas, in the Barents Sea and in the Baffin Bay peak in mid winter (November to February); the East Greenland Current peaks in late winter (February to April). Seasonality is also recognisable in some currents not along the continental slopes. For instance, currents in the Kara Sea (peak between November and January) and in the southern and western branches of the Beaufort Gyre (peak in November-January and March-May respectively).
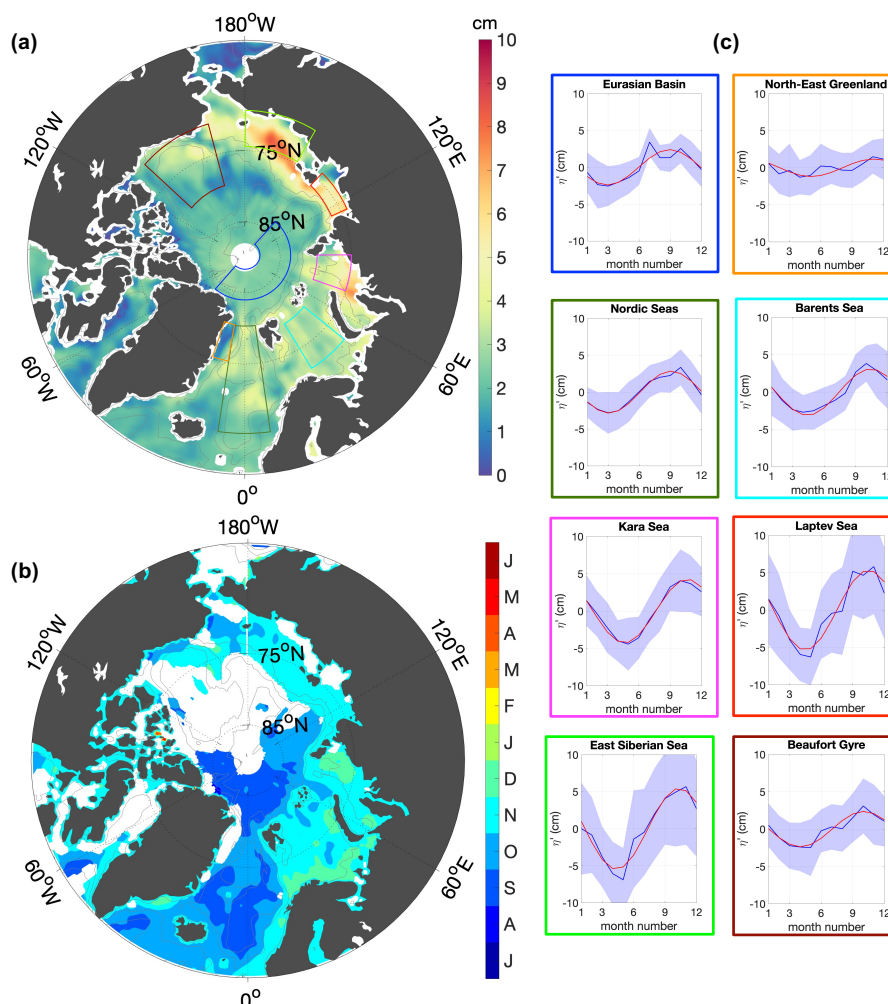
Figure 12. (a) Amplitude and (b) phase of the η' annual harmonic oscillation between 2011 an 2018. Blanked areas in (b) are those areas where the seasonal cycle explains less than 20% of the total variance. Panels in (c) are the η' monthly climatology (blue line, with standard deviation as shading) and the η'_{seas} (red line) averaged over the areas marked in the map with the corresponding color. Bathymetry contours are drawn at 100 m, 1000 m and 2500 m depth.
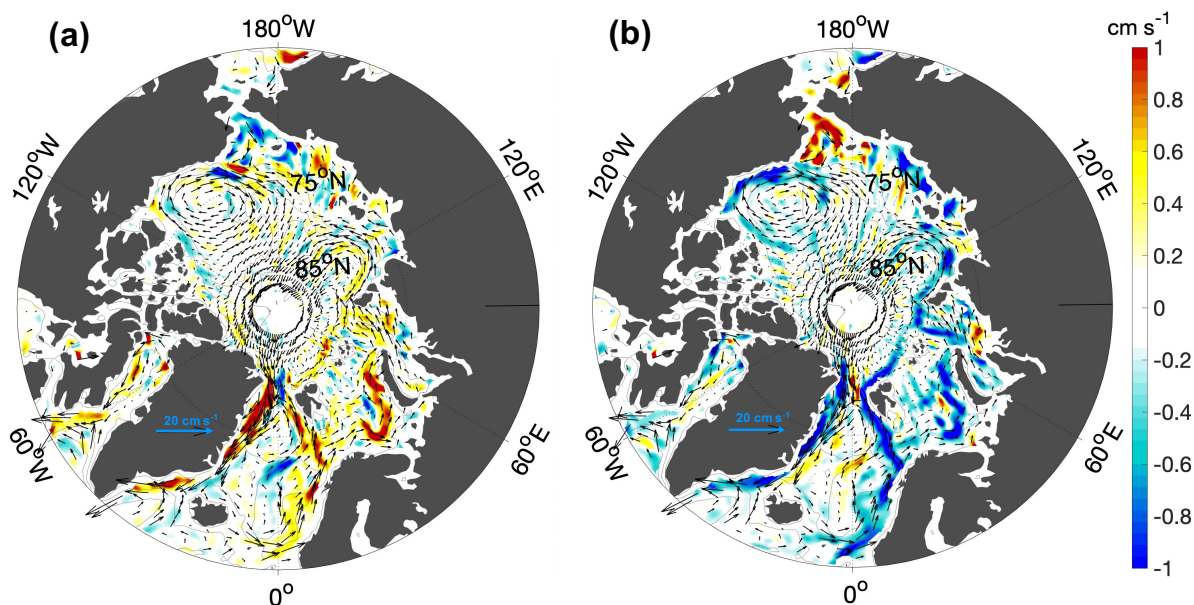
Figure 13. Average (u_g, v_g) fields over the (a) winter months January-February-March and the (b) summer months June-July-August. Bathymetry contours are drawn at 100 m, 1000 m and 2500 m depth. Arrows and colours are to be interpreted as described for Fig. 6c.

6 Discussion

The dataset presented in this paper provides monthly maps of the sea surface height anomaly η' up to 88° N, derived from Cryosat-2 altimetry observations, over the time span of 10 years. In addition, we also provide the associated geostrophic velocity (u_g, v_g), which was not available before north of 82° N. We extensively validated the dataset against independent satellite products and in-situ data in both ice-covered and ice-free regions. In the following, we use results from the validation to discuss (i) the sensitivity of the results to the methodology, (ii) agreement between satellite and in-situ data sources and (iii) the temporal and spatial resolution of our altimetry dataset. Results from a multi-year, Arctic wide comparison of our monthly η' fields against an independent altimetry product showed, despite the general agreement, isolated areas where the correlation between data sets is low. Thus, we discuss whether this is related to the methods used. We also carried out comparisons to in-situ data of both sea surface height and surface velocity. We discuss these results in terms of the spatial and temporal resolution of our altimetry dataset and the underlying dynamic regimes. Finally we put our findings on the seasonal cycle of sea surface height and geostrophic flow in the context of previous literature.

6.1 Impact of methodology

The comparison with the CPOM DOT (Sect. 5.2.1) yielded a correlation higher than 0.7 over 85% of the domain, which indicates that month to month variability is generally robust in relation to the methodology applied. However, in some regions

590 correlation coefficients are lower with non-negligible differences between the datasets. What are the methodological steps that may generate differences between these two data sets?

Regional differences might occur due to different data density, which results from different filtering techniques in the algorithms used for the processing of waveforms. In our comparison the correlation is low in some areas of the ice-covered Arctic. In ice-covered regions the detection of leads is based on surface classification techniques. These differ substantially be-
595 tween studies, depending on the parameters considered or statistical techniques applied, and are to date a source of uncertainty (Dettmering et al., 2018). For instance, more observations are discarded the more conservative a technique is. This yields lower uncertainty, but also lower data density in the central and western Arctic, where the most compact multi year ice is located and lead density is low (Willmes and Heinemann, 2016). Thus, differences in the ice-covered regions can be expected in our comparison, given that Cryosat-2 observations are classified with different parameters and thresholds in the AWI and CPOM
600 datasets (Ricker et al., 2014; Armitage et al., 2016).

Generating data over the marginal ice zone still represents a challenge to overcome. This is because neither ocean-type retrackers nor ice-type retrackers are well suited to process altimetry waveforms there, resulting in noisy or unusable data (Quartly et al., 2019). Thus a smooth transition in the mapped fields depends on the integration of data from ice-free to ice-covered areas, e.g. via interpolation, which is not well constrained by data. It is perhaps not surprising then, that our comparison
605 shows correlation values lower than 0.7 in open ocean areas of the central Arctic and the Baffin Bay, where large patches of low ice concentration form at the end of summer.

We also found that sub-monthly η' variability in the Arctic can yield substantial noise in the monthly gridded fields, especially in the shelf regions (Sect. 4.3.3). To reduce this noise we took two steps. First, we aimed at removing the highest possible fraction of high frequency variability due to ocean tides and the ocean response to pressure plus wind: we tested two correction
610 products for each of these processes and selected the one that removed the most variability. We finally corrected the former using the FES2014 model and the latter using the DAC (Sect. 4.2.2 and Appendices A and B). Second, we applied the DIVA analysis on weekly rather than monthly data input (Sect. 4.3.2). This approach yielded improvements relative the CPOM DOT dataset (applying the FES2004 and IB corrections), especially in regions where the sub-monthly variability is strongest, like in the shelf regions and Baffin Bay (Fig. 5c). For example, in the East Siberian Sea and the Chukchi Sea regions, where we
615 found that the DAC yielded the most improvements over the IB (Appendix B), our monthly η' fields have an average spatial standard deviation of 0.8 cm for the period 2011-2014. This is significantly lower than the corresponding value of 1.0 cm for the same region and period in the CPOM DOT. Furthermore, relatively low correlation values are shown in the Barents Sea and the Baffin Bay, two regions of strong tidal variability where the tidal model FES2014 performs better than the previous version FES2004 (Appendix A; see also Cancet et al., 2018). The lower correlation could thus be attributed to a poorer correction of
620 tidal variability in the CPOM DOT.

6.2 Comparison between satellite altimetry retrievals and in-situ data

The comparison between our altimetry-derived dataset and in situ data showed that agreement between these two data sources can be expected at scales larger than about 50 km. Large scale patterns of altimetry-derived dynamic ocean topography are

consistent with hydrography-based sea surface height in the central Arctic and in the Fram Strait, and show continuity across the
625 ice edge (Fig. 2b and 8). On the other hand, we note that altimetry is unable to resolve scales shorter than 50 km in the Fram
Strait when comparing monthly profiles to snapshots from hydrographic sections. Pointwise comparison with independent
in-situ sea surface height from mooring data were used to assess the time variability of our altimetry product in two separate
regions of the central Arctic, the Fram Strait and the Nansen Basin. Results showed that altimetry and in-situ data yield roughly
consistent patterns and exhibit variability on similar time scales, e.g. a clear seasonal signal in the Fram Strait and at the Laptev
630 Sea continental slope, and enhanced monthly variability in the Nansen Basin.

Correlation values between altimetry and mooring sea surface height observations from the open ocean (Fig. 9) were lower
or comparable to previous studies which compared altimetry and near-shore tide gauge measurements (Volkov and Pujol,
2012; Armitage et al., 2016; Rose et al., 2019). This can be expected given that tide gauges measure sea surface height, directly
comparable to altimetry. Conversely, when estimating sea surface height from mooring data, uncertainties arise as a result of
635 limited vertical resolution of density observations. In our case, we did find the highest correlation with the mooring data with
the most continuous and extended vertical sampling (M_4p6). Furthermore, we expect tide gauge measurements to correlate
better with altimetry given that sea surface height variability near the coast shows larger amplitudes than in the open ocean (see
Fig. 12). Nevertheless, the RMSD between altimetry and open ocean mooring observations (2.6-3.8 cm) was consistent with
other studies comparing altimetry to in-situ observations. For instance, RMSD values in the range of 2 to 12 cm have been
640 found both from the comparison of altimetry data with tide gauges across the Arctic (Volkov and Pujol, 2012; Armitage et al.,
2016; Rose et al., 2019) and with steric height measured in the Arctic Deep Basins (Kwok and Morison, 2011). Another study
by Armitage et al. (2017) compared altimetry-derived currents with moored currents velocity from the interior of the Beaufort
Sea. Correlation values in Armitage et al. (2017) were lower or equal to 0.54, in line with our findings at most mooring sites,
except for mooring M1_1 which shows higher correlation (0.77). The RMSD values of 1-2 cm s^{-1} over currents of 1-6 cm s^{-1}
645 also agrees well with the RMSD that we find in the interior of the Eurasian Basin (1.1-2.0 cm s^{-1}).

6.3   Temporal and spatial resolution of altimetry-derived currents

The large spatial extent of mooring velocity measurements and their long deployment period allows us to examine the corre-
lation of altimetry and in-situ velocity over different dynamic regimes and spatio-temporal scales. We found that correlation is
higher in regions where the flow variability is dominated by steady currents (i.e. boundary currents) and lower where it is domi-
650 nated by nonstationary eddy activity. In the Fram Strait, altimetry and in-situ data show the highest correlation on the shore and
continental slope east of 5°E, within the West Spitsbergen Current, with maximum correlation in the core, non-eddying part
of the current (mooring F3, Beszczynska-Möller et al., 2012). In the Laptev Sea the correlation is highest at mooring M1_1,
close to the shelf break, where the the Arctic Boundary Current is strongest (Aksenov et al., 2011; Baumann et al., 2018). On
the contrary, in both regions the correlation breaks down where mean currents are slow and the mesoscale activity is enhanced.
655 Namely, the correlation is low and non significant at moorings in the central Fram Strait, where the surface circulation is
dominated by westward eddies propagation (von Appen et al., 2016; Hattermann et al., 2016). Similarly, correlation was low
in the offshore part of the Laptev Sea continental slope, where current speed is low and eddy activity increases (Pnyushkov

et al., 2015, 2018; Baumann et al., 2018). The correlation varies with the dynamic regime due to the different sampling of
mesoscale activity by moorings and by altimetry. Mesoscale features are not resolved in our monthly altimetry fields because
660   of the 50 km smoothing scale used in the interpolation. This is equivalent to about ten times the local first mode baroclinic
Rossby radius (Nurser and Bacon, 2014; von Appen et al., 2016; Pnyushkov et al., 2015), which roughly sets the horizontal
scale of mesoscale eddies.

We thus used in-situ surface velocities to evaluate the effective spatial and temporal resolution of altimetry-derived monthly
currents. In the region of the West Spitsbergen Current, the correlation between altimetry and in-situ varies depending on the
665   horizontal distance over which velocity is averaged. On the one hand, the correlation is higher when averaging over about 50
km relative to about 20 km (compare test 1 and 2 in Table 5). This indicates that the boundary current variability as observed
by our altimetry-derived velocity agree most closely with the in-situ observed variability when both are averaged across at
least 50 km. On the other hand, slightly lower correlation values are obtained when averaging data further into the central Fram
Strait (see test 3 in Table 5), due to the different dynamic regime. There, eddies are a source of variability at intra-seasonal
670   time scales, which is not resolved by our altimetry maps and which biases the large-scale average velocity from moorings. By
low-pass filtering velocities with a cutoff of 4 months, we found, indeed, that the correlation between altimetry and in-situ data
is increased both in the Fram Strait and at the Laptev Sea continental slope.

The considerations above suggest that our monthly geostrophic velocities can resolve seasonal to interannual variability of
boundary currents wider than about 50 km. Mesoscale intra-seasonal variability is, however, not resolved. In a recent study,
675   Prandi et al. (2021) achieved a temporal resolution of 1.5 months in the Arctic Ocean, over a time span of three years, by
using data from more than one satellite. Other studies in the past, including other seas, found that multi-altimeter integration
is necessary to resolve mesoscale activity (e.g., Pujol et al., 2010). This indicates that future efforts to increase the temporal
resolution of gridded altimetry products should be directed towards the integration of data from more than one satellite. This
comes however at the expense of the duration of the time series, which is limited to the period when satellites' activity overlap.

680   ## 6.4   Seasonality

The sea surface height seasonal cycle is driven by changes in the steric component (due to vertical buoyancy fluxes and
advection) and the mass component (due to water accumulation or release, precipitation, evaporation, river runoff). Previous
studies identified the seasonal cycle as the dominant component of the sea surface height variability in the Arctic (e.g., Volkov
et al., 2013; Armitage et al., 2016; Müller et al., 2019). Our results confirm these findings, showing that this variability explains
685   a fraction higher than 20% of the total variability in large areas of the Arctic, including the Arctic Shelves, the Nordic Seas,
the Eurasian Basin and part of the Canada Basin. Additionally, from monthly time series of altimetry-derived and in-situ
geostrophic velocity we found that the variability of boundary currents at seasonal to interannual timescales dominates over
intra-seasonal variability.

Large scale features emerge in the seasonal cycle of η' and (u_g, v_g). First, η' has seasonal maximum in winter, between
690   September and December, over most of the Arctic. Furthermore, we found that the amplitude of the seasonal cycle of η',
as well as the fraction of variability explained, are higher over the shelf regions than in open ocean regions of the Arctic

Table 6. Time of seasonal maximum occurrence in the currents of the Arctic Ocean in the results of this study. The acronym of currents correspond to those indicated in Fig. 1 and slope currents are marked in bold. The third column indicate previous studies that find seasonality in agreement with our results.

Current	Time of seasonal maximum	Other studies
WSC (and NwASC)	November to February	Beszczynska-Möller et al. (2012); von Appen et al. (2016)
BSB	November to February	Schauer et al. (2002)
VSC	November to December	Janout et al. (2015)
ABC	October to January (western Nansen Basin)	Pérez Hernández et al. (2019)
	September to December (Laptev Sea continental Slope)	Baumann et al. (2018)
BG	October to January (southern branch)	Proshutinsky et al. (2009); Armitage et al. (2017)
	March to May (western branch)	Min et al. (2019)
EGC	February to April	Bacon et al. (2014); Le Bras et al. (2018); de Steur et al. (2018)

interior. Lastly, we found that geostrophic currents consistently strengthen along the continental slopes in winter and weaken in summer. These features find support in the literature. The wintertime occurrence of the η' seasonal maximum is in agreement with previous studies of steric height seasonality from in-situ data. For instance, from hydrographic profiles, the steric height

695 was found to peak between September and November in the Greenland and Norwegian Seas (Siegismund et al., 2007), in the central Barents Sea (Volkov et al., 2013) and in the Canada Basin (Proshutinsky et al., 2009). Besides, the secondary peak appearing from the η' climatology in most of the Arctic interior (Fig. 12c) is in agreement with the late summer peak of ocean mass found by Peralta-Ferriz and Morison (2010) from GRACE data. Overall, both the Arctic-wide occurrence of the winter maximum and the decoupling of shallow and deep regions agree well with the two first Empirical Orthogonal Functions of sea

700 surface height derived by Bulczak et al. (2015) and Armitage et al. (2016): a basin-wide oscillation with a wintertime maximum and an anti-phase oscillation between shelf regions and deep basins. Finally, the strengthening of boundary currents in winter was documented for several regions by previous studies based on in-situ data, satellite data and model output (Table 6). Our dataset is thus able to describe the seasonality of sea surface height and geostrophic currents across the Arctic, consistent with previous studies.

705 **7 Conclusions**

With this work we aim to contribute to basin scale observational studies of the Arctic Ocean circulation by providing a new Arctic-wide gridded product of satellite-derived sea surface height anomaly (η') and geostrophic velocity (u_g, v_g). We present

Arctic-wide monthly maps of η' and (u_g, v_g), spanning the years 2011 to 2020, covering both the ice-free and ice-covered parts of the ocean. We believe that this dataset can be used to study variability with spatial scales above 50 km, at seasonal to
710 interannual time scales.

We find that sub-monthly variability in the Arctic Ocean, due to tides and the response to wind and pressure, is a source of noise in the η' monthly fields. We reduced this noise by using tailored altimetry corrections and interpolating weekly subsets of data. The comparison of our dataset with the independent altimetry dataset CPOM DOT at monthly timescales indicates that altimetry-derived sea surface height variability is fairly robust with respect to the methodology applied.

715 Altimetry-derived temporal variability shows agreement with mooring data at seasonal and longer time scales, while differences persist at monthly time scales. The correlation between altimetry and moored velocity is highest at mooring sites within boundary currents both in the Fram Strait (0.54) and at the Laptev Sea continental slope (0.77). The agreement varies depending on the underlying nature and scales of the variability, showing the highest correlation in regions where a stable flow (e.g. boundary currents) dominates the mesoscale eddy activity.

720 Lastly, large scale patterns emerge from a preliminary analysis of the seasonality: η' exhibits a basin-wide coherent seasonal cycle, with a wintertime maximum and higher amplitude on the shelves; the (u_g, v_g) features an intensification of the Arctic slope currents in winter and a weakening in summer. The agreement of these features with previous in-situ based studies points to the important role that altimetry has in the Arctic Ocean, integrating individual mooring-inferred results into a basin-wide perspective.

725 **8   Data availability**

The final monthly maps of sea surface height anomaly and geostrophic velocity (2011-2018) is available at https://doi.pangaea.de/10.1594/PANGAEA.931869 (Doglioni et al., 2021b, currently under moratorium). A token for temporary access to the data for reviewers can be generated at https://www.pangaea.de/tok/af2fadcef01bc9830a67e1d522e47193c2e01946. This data file includes also, as auxiliary fields: $i)$ the relative error on the sea surface height; $ii)$ the mean dynamic topography
730 for the period 2011-2020; $iii)$ monthly binned values of along track sea surface height anomaly derived as described in Sect. 4.2 of this manuscript.

The time series of steric height and bottom pressure equivalent height at moorings FS_S, AC and M1_4p6, as processed in this work, are available at https://doi.pangaea.de/10.1594/PANGAEA.931871 (Doglioni et al., 2021c), https://doi.pangaea.de/10.1594/PANGAEA.931878 (Doglioni et al., 2021a), and
735 https://doi.pangaea.de/10.1594/PANGAEA.931875 (Doglioni et al., 2021d), respectively.
All data are under moratorium and tokens for temporary access to the data for reviewers can be generated at https://www.pangaea.de/tok/452d4f0de47d5ce052d2d034c530e5411f9eaeea (FS_S),
https://www.pangaea.de/tok/b0bc5a83d50afd2895eeae4fa7b56f92390da17c (AC),
and https://www.pangaea.de/tok/2eb57291ca176992308db663044212325483cab3 (M1_4p6).

Appendix A: Ocean Tides Correction

Following the European Space Agency indications (European Space Agency, 2016; Lyard et al., 2006), tidal variability has in the past been corrected using the standard tidal model FES2004 or equally performing models (e.g., Pujol et al., 2016; Mizobata et al., 2016; Armitage et al., 2016; Müller et al., 2019). Recent works (e.g., Rose et al., 2019; Prandi et al., 2021) have instead used new model versions with improved performance (Cancet et al., 2018) such as the FES2014 model (Lyard et al., 2021). In order to see what is the support our choice to use FES2014 over FES2004, we compared their performance by evaluating the difference in residual noise on the monthly maps due to unresolved submonthly variability (computed as in Sect. 4.3.3).

We display here in Fig A1 the submonthly contribution to the standard error in two areas of high tidal amplitude, namely the Barents Sea and the Baffin Bay. We note that, in both regions, FES2014 reduces the standard error of values up to 0.3-0.5 cm with respect to FES2004 (Fig. A1c and A1f), which is about 20% of its local value and 30%-50% of the average value over the whole Arctic. In agreement with these results, findings from Cancet et al. (2018), who compared the performances of several tidal models in the Arctic, show that differences in tidal amplitude and phase with respect to tide gauge data are much lower for FES2014 than for FES2004.
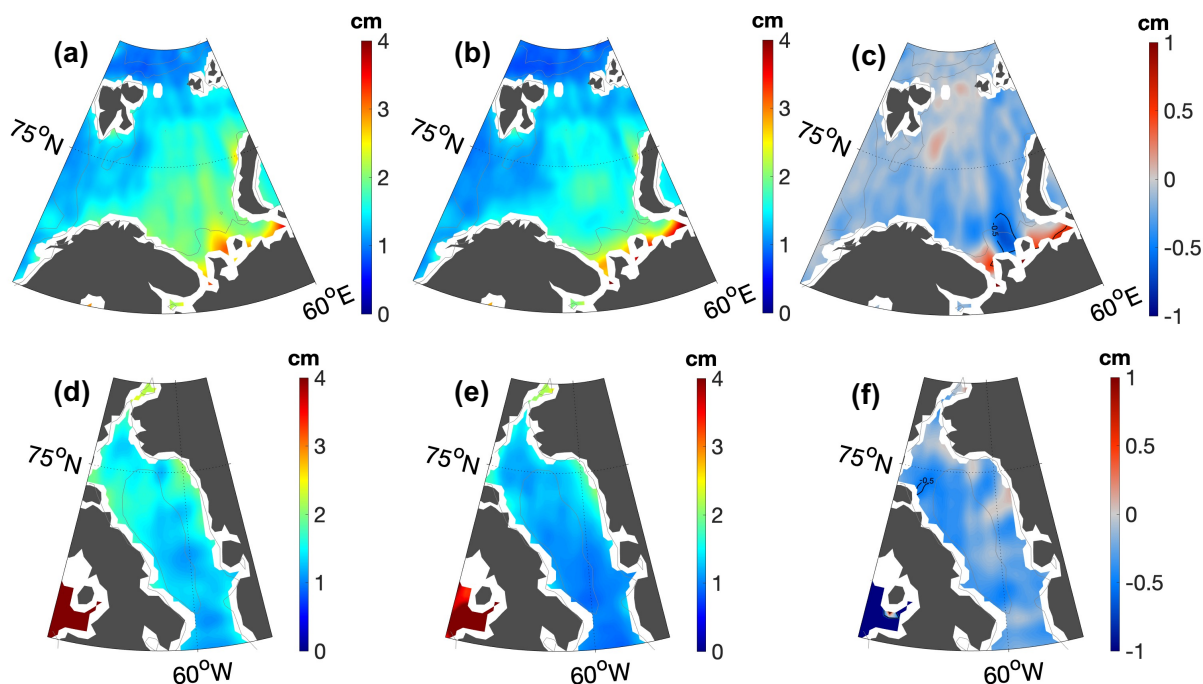
Figure A1. Comparison of performance of FES2004 and FES2014-based corrections. Submonthly contribution to the standard error on monthly η' maps in the Barents Sea (a, b, c) and Baffin Bay (d, e, f) when using the tidal correction FES2004 (a, d) and FES2014 (b, c). In panels (e) and (f) is shown the reduction in the error obtained with FES2014 with respect to FES2004.

Appendix B: Dynamic Atmospheric Correction

755 The DAC corrects the local and the dynamic ocean response (waves) to pressure and wind changes and is derived from the sea surface height output of a barotropic model (Carrère and Lyard, 2003; Carrère et al., 2016). Up until the early 2000s, the effect of atmospheric pressure and winds on sea surface height had instead been corrected using an Inverse Barometer formula (IB, e.g., Ponte and Gaspar (1999); Carrère and Lyard (2003)). In the IB assumption, the sea surface height responds locally to changes in pressure, decreasing of approximately 1 cm for each increase in pressure of 1 mbar (atmospheric loading). Even

760 though it has been shown that the IB is not always a good approximation of the ocean response, especially on time scales shorter than 20 days (Carrère and Lyard, 2003), little is known of what is the response in ice-covered regions (Robbins et al., 2016).

Table B1. Standard deviations of the three time series of along-track η', averaged over the East Siberian Sea box (Fig. B1), using uncorrected η', η' corrected by IB and η' corrected by DAC. For each year only ice-covered data are used, in the months November-July. Standard deviations are presented for the time series filtered in three different frequency bands.

standard deviation (cm) [uncorrected / IB / DAC]	T > 20 days	20 days > T > 5 days	T < 5 days
2011-2012	16.2 / 14.3 / 13.3	9.3 / 9.2 / 5.8	3.1 / 3.4 / 2.2
2012-2013	14.7 / 10.8 / 9.7	8.9 / 9.7 / 4.8	3.2 / 3.7 / 2.2
2013-2014	12.0 / 12.5 / 9.9	8.5 / 9.1 / 4.0	3.2 / 3.6 / 2.4
2014-2015	7.3 / 8.0 / 7.7	9.3 / 9.9 / 4.5	2.4 / 2.9 / 1.9
2015-2016	19.3 / 15.7 / 15.7	7.3 / 7.8 / 3.6	3.0 / 3.6 / 2.2
2016-2017	15.3 / 13.5 / 13.1	8.8 / 9.7 / 4.4	3.2 / 4.0 / 2.3
2017-2018	10.0 / 7.4 / 6.8	9.2 / 11.0 / 4.8	3.4 / 3.8 / 2.5
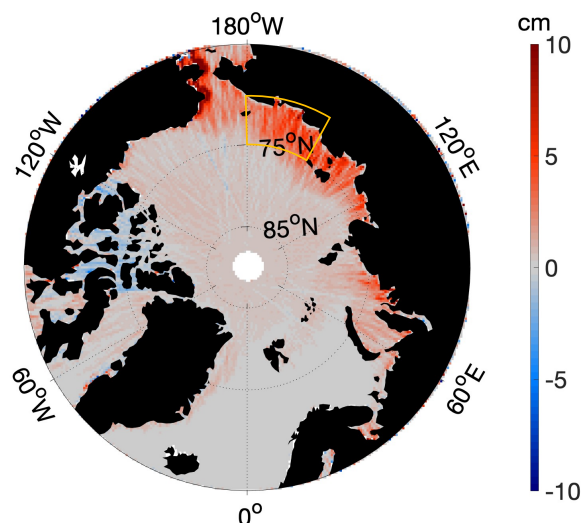
Figure B1. The along track improvement of DAC correction, with respect to IB, in removing η' high frequency variability. Colours indicate the difference between the standard deviation of along track η' corrected IB and corrected with DAC. The yellow square indicate the region of the East Siberian Sea where the frequency analysis was performed.
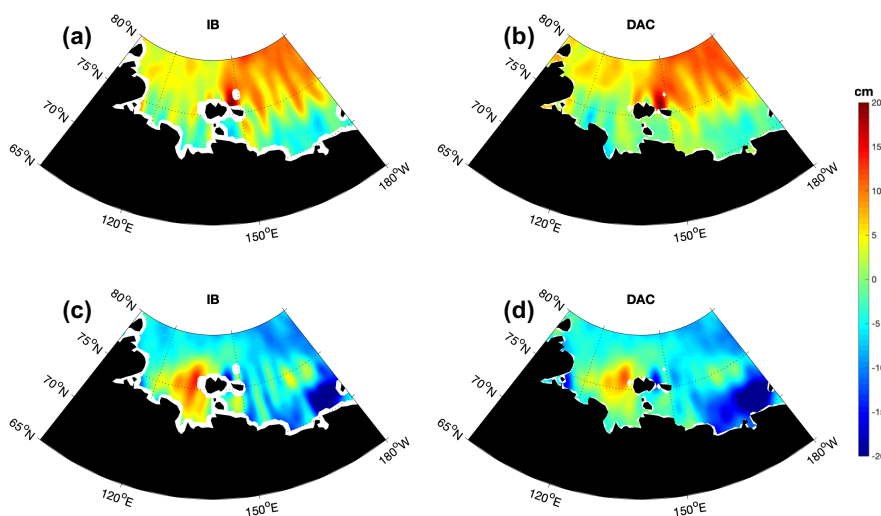
Figure B2. Effect of using correction DAC (panels (b) and (d)) instead of IB (panels (a) and (c)) on the monthly gridded η' fields (see Sect. 4.3). Two examples are shown for the months of November 2014 (panels (a) and (b)) and November 2017 (panels (c) and (d)).

To establish whether DAC should be used also in ice covered regions, we compared the reduction in altimetry standard deviation obtained by applying DAC with respect to IB in ice-covered regions of the Arctic Ocean. Fig. B1a shows the binned

765   difference in standard deviation applying the two corrections, where positive values indicate better performance of DAC over IB. The DAC outperforms the IB in shallow shelf regions, and the two corrections perform equally well over the deep basins.

To understand which frequency bands have mostly contributed to this improvement, we took as an example the East Siberian Sea (yellow square indicated in Fig. B1a). We generated three time series of uncorrected η', η' corrected by IB and η' corrected by DAC, averaged with timestep of 1 day over the indicated region. For each year we analysed periods between November and

770   July, which are the only months when data from leads are available. For each time series, we computed the standard deviation in frequency bands with periods T > 20 days, 5 days < T < 20 days, T < 5 days (Table B1). Results show that DAC reduced the uncorrected η' standard deviation by 50% at periods shorter than 20 days, in contrast to no reduction when applying a simple IB.

Furthermore, standard deviation at periods between 20 days and 5 days is larger then 60% the standard deviation at periods

775   longer than 20 days, confirming that high frequency variability represent a high portion of the total variability in the Arctic Ocean. The improvement of DAC with respect to IB over the shelves appears also in the η' monthly grids, where meridionally oriented patterns of η' are evidently reduced (two examples are given for the months of November 2014 and November 2017 in Fig. B2).

Appendix C: Aliasing of residual sub-monthly variability

780   As stated in the main text, we performed the interpolation on weekly data subsets of observations of η'. Monthly maps were then obtained as the average of four weekly maps. The reasoning behind our approach is based on the fact that sea surface height in the Arctic exhibit large-scale, high frequency (sub-monthly) variability, associated in part to the fast propagation of large-scale barotropic waves across the Arctic (Peralta-Ferriz et al., 2011; Fukumori et al., 2015; Danielson et al., 2020). This means that the variability is spatially coherent over hundreds of kilometers, yet it decorrelates quickly over time (e.g. weeks).

785   Thus, measurements taken along tracks that are far away from each other, yet within a few days from each other, may still be able to resolve to some extent the spatial-temporal characteristics of the ocean variability. Instead, measurements taken along tracks that are close to each other, yet taken two weeks apart from each other, will create stripes (strong spatial sea surface height gradients) by not resolving the temporal variability. Since Cryosat-2 samples close-by regions at times separated by a large gap over the course of a month, trackiness will occur.

790   Therefore, constructing monthly maps based on sampling this large scale, high frequency variability at different times in different locations, will artificially produce short wavelength patterns. We demonstrate this effect exemplarily in Fig C1. One can clearly see how the sudden change in the large scale sea surface height between the first and the following weeks produces artificial stripes in the map when the monthly subset of data is interpolated.
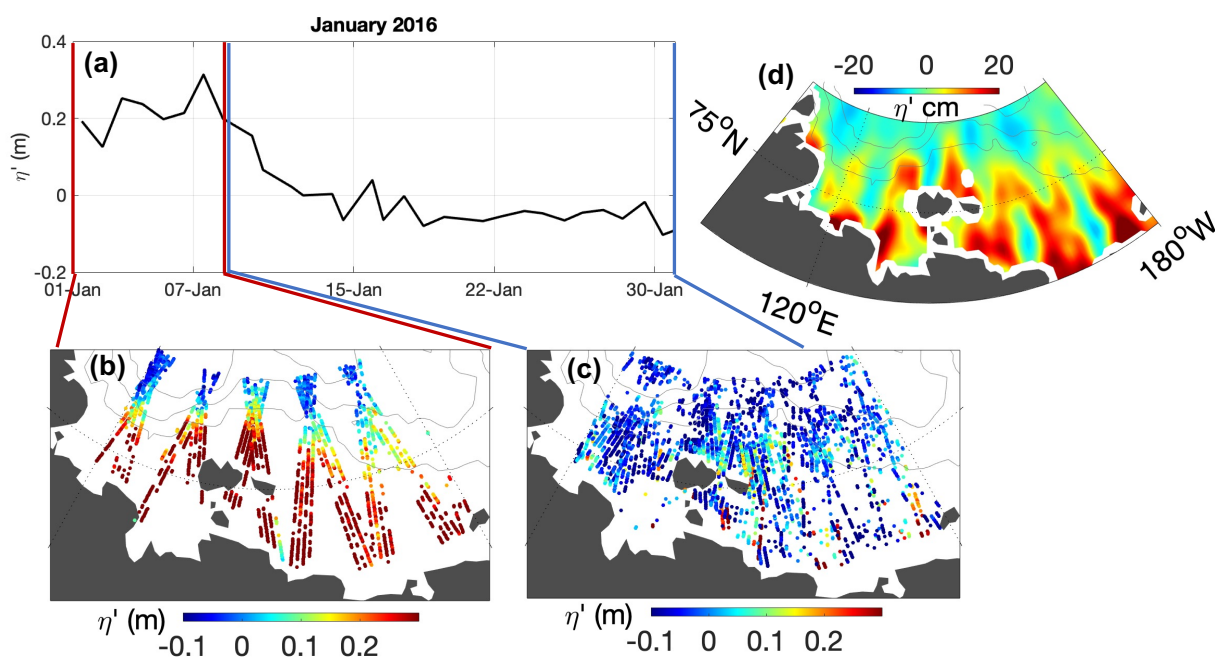
Figure C1. Trackiness introduced by sub-monthly variability. (a) Time series of average along track η' in the East Siberian and Laptev Sea for the month of January 2016. Bottom panels: scattered along track η' in the periods of (b) 1-8 January and (c) 9-31 January. (d) η' field for the month of January 2016 if interpolation is performed on a monthly set of observations.

Author contributions. FD processed the along-track data, performed the interpolation and the comparisons, wrote most of the text. RR
795   provided the along-track observations in the ice-covered regions and supported the processing of those. BR contributed to the processing
of part of the in-situ data and to the discussion and application of the interpolation method. AB and CT contributed to the application and
description of the DIVA method. TK supervised the work and advised on the comparison with in-situ data. All authors contributed to the
discussion of the results and to the improvement of the manuscript.

Competing interests. The authors declare that they have no conflict of interest.

800   *Acknowledgements.* The processing of the CryoSat-2 sea surface height in ice-covered regions was funded by the German Ministry of Eco-
nomics Affairs and Energy (grant: 50EE1008); data from 2011 to 2018 were obtained from https://www.meereisportal.de (grant:REKLIM-
2013-04). In-situ temperature and salinity data, ocean bottom pressure records and velocity data are available in the framework of the
Helmholtz society strategic investment FRontiers in Arctic marine Monitoring (FRAM) as well as the Nansen and Amundsen Basins Obser-
vations System II program (NABOS-II, NSF grants AON-1203473, AON-1338948, and 1708427) and the joint Russian-German research
805   project Changing Arctic Transpolar System (CATS). We are thankful to these projects for making publicly available quality controlled in-situ
data. We thank expressly Vladimir Ivanov for leading the research expeditions of the CATS and NABOS-II project and making the data col-
lection possible. The work of FD, TK and BR was part of the cooperative project REgional Atlantic Circulation and global changE (RACE)
funded by the German Federal Ministry for Education and Research (BMBF), grant ID #03F0824E. The work of FD is a contribution to
the "Helmholtz Climate Initiative REKLIM," a joint research project by the Helmholtz Association of German research centres (HGF).
810   The work of BR further contributed to the project Advective Pathways of nutrients and key Ecological substances in the Arctic (APEAR)
project (NE/R012865/1, NE/R012865/2, #03V01461), part of the Changing Arctic Ocean programme, jointly funded by the UKRI Natural
Environment Research Council (NERC) and the German Federal Ministry of Education and Research (BMBF).

References

Aksenov, Y., Ivanov, V. V., Nurser, A. J. G., Bacon, S., Polyakov, I. V., Coward, A. C., Naveira-Garabato, A. C., and Beszczynska-Moeller,
815   A.: The Arctic Circumpolar Boundary Current, Journal of Geophysical Research, 116, 11, https://doi.org/10.1029/2010JC006637, 2011.

Alexandrov, V., Sandven, S., Wahlin, J., and Johannessen, O. M.: The relation between sea ice thickness and freeboard in the Arctic, The
    Cryosphere, 4, 373–380, https://doi.org/10.5194/tc-4-373-2010, 2010.

Andersen, O., Knudsen, P., and Stenseng, L.: The DTU13 MSS (Mean Sea Surface) and MDT (Mean Dynamic Topography) from 20 Years
    of Satellite Altimetry, in: IGFS 2014, pp. 111–121, Springer, Cham, Cham, https://doi.org/10.1007/1345_2015_182, 2015.

820   Armitage, T. W. K. and Davidson, M. W. J.: Using the Interferometric Capabilities of the ESA CryoSat-2 Mission to Im-
    prove the Accuracy of Sea Ice Freeboard Retrievals. , IEEE Transactions on Geoscience and Remote Sensing, 52, 529–536,
    https://doi.org/10.1109/TGRS.2013.2242082, 2014.

Armitage, T. W. K., Bacon, S., Ridout, A. L., Thomas, S. F., Aksenov, Y., and Wingham, D. J.: Arctic sea surface height variabil-
    ity and change from satellite radar altimetry and GRACE, 2003-2014, Journal of Geophysical Research: Oceans, 121, 4303–4322,
825   https://doi.org/10.1002/2015JC011579, 2016.

Armitage, T. W. K., Bacon, S., Ridout, A. L., Petty, A. A., Wolbach, S., and Tsamados, M.: Arctic Ocean surface geostrophic circulation
    2003–2014, The Cryosphere, 11, 1767–1780, https://doi.org/10.5194/tc-11-1767-2017, 2017.

Bacon, S., Marshall, A., Holliday, N. P., Aksenov, Y., and Dye, S. R.: Seasonal variability of the East Greenland Coastal Current, Journal of
    Geophysical Research: Oceans, 119, 3967–3987, https://doi.org/10.1002/2013JC009279, 2014.

830   Barth, A., Beckers, J. M., Troupin, C., Alvera-Azcárate, A., and Vandenbulcke, L.: divand-1.0: n-dimensional variational data analy-
    sis for ocean observations, Geoscientific Model Development, 7, 225 – 241, https://doi.org/10.5194/gmd-7-225-2014, https://www.
    geosci-model-dev.net/7/225/2014/, 2014.

Barth, A., Troupin, C., Reyes, E., Alvera-Azcárate, A., Beckers, J.-M., and Tintoré, J.: Variational interpolation of high-frequency radar
    surface currents using DIVAnd, Ocean Dynamics, 71, 293–308, https://doi.org/10.1007/s10236-020-01432-x, 2021.

835   Baumann, T. M., Polyakov, I. V., Pnyushkov, A. V., Rember, R., Ivanov, V. V., Alkire, M. B., Goszczko, I., and Carmack, E. C.: On the
    Seasonal Cycles Observed at the Continental Slope of the Eastern Eurasian Basin of the Arctic Ocean, Journal of Physical Oceanography,
    48, 1451–1470, https://doi.org/10.1175/JPO-D-17-0163.1, 2018.

Beckers, J.-M., Barth, A., Troupin, C., and Alvera-Azcárate, A.: Approximate and Efficient Methods to Assess Error Fields in Spa-
    tial Gridding with Data Interpolating Variational Analysis (DIVA), Journal of Atmospheric and Oceanic Technology, 31, 515 – 530,
840   https://doi.org/10.1175/jtech-d-13-00130.1, 2014.

Belgacem, M., Schroeder, K., Barth, A., Troupin, C., Pavoni, B., Raimbault, P., Garcia, N., Borghini, M., and Chiggiato, J.: Climatological
    distribution of dissolved inorganic nutrients in the western Mediterranean Sea (1981–2017), Earth System Science Data, 13, 5915–5949,
    https://doi.org/10.5194/essd-13-5915-2021, 2021.

Beszczynska-Möller, A., Fahrbach, E., Schauer, U., and Hansen, E.: Variability in Atlantic water temperature and transport at the entrance to
845   the Arctic Ocean, 1997–2010, ICES Journal of Marine Science, 69, 852–863, https://doi.org/10.1093/icesjms/fss056, 2012.

Birol, F., Fuller, N., Lyard, F., Cancet, M., Niño, F., Delebecque, C., Fleury, S., Toublanc, F., Melet, A., Saraceno, M., and Léger, F.:
    Coastal applications from nadir altimetry: Example of the X-TRACK regional products, Advances in Space Research, 59, 936–953,
    https://doi.org/10.1016/j.asr.2016.11.005, 2017.

Bouffard, J., Naeije, M., Banks, C. J., Calafat, F. M., Cipollini, P., Snaith, H. M., Webb, E., Hall, A., Mannan, R., Féménias,
850   P., and Parrinello, T.: CryoSat ocean product quality status and future evolution, Advances in Space Research, 62, 1549–1563,
        https://doi.org/10.1016/j.asr.2017.11.043, 2017.

Bouzinac, C.: CryoSat Product Handbook, Tech. rep., European Space Agency, https://earth.esa.int/documents/10174/125272/CryoSat_
        Product_Handbook, 2012.

Brasseur, P., Beckers, J., Brankart, J., and Schoenauen, R.: Seasonal temperature and salinity fields in the Mediterranean Sea: Climatological
855   analyses of a historical data set, Deep Sea Research Part I: Oceanographic Research Papers, 43, 159–192, https://doi.org/10.1016/0967-
        0637(96)00012-x, 1996.

Brasseur, P. P. and Haus, J. A.: Application of a 3-D variational inverse model to the analysis of ecohydrodynamic data in the Northern
        Bering and Southern Chukchi Seas, Journal of Marine Systems, 1, 383–401, https://doi.org/10.1016/0924-7963(91)90006-g, 1991.

Bretherton, F. P., Davis, R. E., and Fandry, C. B.: A technique for objective analysis and design of oceanographic experiments applied to
860   MODE-73, Deep Sea Research, 23, 559–582, https://doi.org/10.1016/0011-7471(76)90001-2, 1976.

Bruinsma, S. L., Förste, C., Abrikosov, O., Lemoine, J.-M., Marty, J.-C., Mulet, S., Rio, M. H., and Bonvalot, S.: ESA's satellite-
        only gravity field model via the direct approach based on all GOCE data, Geophysical Research Letters, 41, 7508–7514,
        https://doi.org/10.1002/2014GL062045, 2014.

Bulczak, A. I., Bacon, S., Garabato, A. C. N., Ridout, A., Sonnewald, M. J. P., and Laxon, S. W.: Seasonal variability of sea surface height in
865   the coastal waters and deep basins of the Nordic Seas, Geophysical Research Letters, 42, 113–120, https://doi.org/10.1002/(ISSN)1944-
        8007, 2015.

Cancet, M., Andersen, O. B., Lyard, F., Cotton, D., and Benveniste, J.: Arctide2017, a high-resolution regional tidal model in the Arctic
        Ocean, Advances in Space Research, 62, 1324 – 1343, https://doi.org/10.1016/j.asr.2018.01.007, https://www.sciencedirect.com/science/
        article/pii/S0273117718300309#f0005, 2018.

870   Capet, A., Troupin, C., Carstensen, J., Grégoire, M., and Beckers, J.-M.: Untangling spatial and temporal trends in the variability of the
        Black Sea Cold Intermediate Layer and mixed Layer Depth using the DIVA detrending procedure, Ocean Dynamics, 64, 315–324,
        https://doi.org/10.1007/s10236-013-0683-4, 2014.

Carrère, L. and Lyard, F.: Modeling the barotropic response of the global ocean to atmospheric wind and pressure forcing - comparisons with
        observations, Geophysical Research Letters, 30, 405, https://doi.org/10.1029/2002GL016473, 2003.

875   Carrère, L., Faugère, Y., and Ablain, M.: Major improvement of altimetry sea level estimations using pressure-derived corrections based on
        ERA-Interim atmospheric reanalysis, Ocean Science, 12, 825–842, https://doi.org/10.5194/os-12-825-2016, 2016.

Cartwright, D. E. and Edden, A. C.: Corrected Tables of Tidal Harmonics, Geophysical Journal International, 33, 253–264.,
        https://doi.org/https://doi.org/10.1111/j.1365-246X.1973.tb03420.x, 1973.

Danielson, S. L., Hennon, T. D., Hedstrom, K. S., Pnyushkov, A. V., Polyakov, I. V., Carmack, E. C., Filchuk, K., Janout, M., Makhotin, M.,
880   Williams, W. J., and Padman, L.: Oceanic Routing of Wind-Sourced Energy Along the Arctic Continental Shelves, Frontiers in Marine
        Science, 7, 815, https://doi.org/10.3389/fmars.2020.00509, 2020.

de Steur, L., Hansen, E., Gerdes, R., Karcher, M., Fahrbach, E., and Holfort, J.: Freshwater fluxes in the East Greenland Current: A decade of
        observations, Geophysical Research Letters, 36, 14 485, https://doi.org/10.1029/2009GL041278, https://agupubs.onlinelibrary.wiley.com/
        doi/full/10.1029/2009GL041278, 2009.

885   de Steur, L., Peralta-Ferriz, C., and Pavlova, O.: Freshwater Export in the East Greenland Current Freshens the North Atlantic, Geophysical
        Research Letters, 45, 13,359–13,366, https://doi.org/10.1029/2018GL080207, 2018.

Dettmering, D., Wynne, A., Müller, F. L., Passaro, M., and Seitz, F.: Lead Detection in Polar Oceans—A Comparison of Different Classification Methods for Cryosat-2 SAR Data, Remote Sensing, 10, 1190, https://doi.org/10.3390/rs10081190, 2018.

Doglioni, F., Ivanov, V., Ricker, R., Rabe, B., and Kanzow, T.: Steric height and bottom pressure water equivalent derived from mooring data at the shelf break north of the Arctic Cape., https://doi.pangaea.de/10.1594/PANGAEA.931878, 2021a.

Doglioni, F., Ricker, R., Rabe, B., and Kanzow, T.: Pan-Arctic monthly maps of sea surface height anomaly and geostrophic velocity from the satellite altimetry Cryosat-2 mission, 2011-2020, https://doi.pangaea.de/10.1594/PANGAEA.931869, 2021b.

Doglioni, F., Ricker, R., Rabe, B., and Kanzow, T.: Steric height and bottom pressure water equivalent derived from mooring data in the Fram Strait., https://doi.pangaea.de/10.1594/PANGAEA.931871, 2021c.

Doglioni, F., Ricker, R., Rabe, B., and Kanzow, T.: Steric height and bottom pressure water equivalent derived from mooring data at the shelf break north of the Arctic Cape., https://doi.pangaea.de/10.1594/PANGAEA.931878, 2021d.

Emery, W. J. and Thomson, R. E.: Chapter 3 - Statistical Methods and Error Handling, in: Data Analysis Methods in Physical Oceanography, edited by Emery, W. J. and Thomson, R. E., pp. 193–304, Elsevier Science, Amsterdam, https://doi.org/https://doi.org/10.1016/B978-044450756-3/50004-6, 2001.

European Space Agency: Geophysical Corrections in Level 2 CryoSat Data Products, Tech. Rep. IDEAS-VEG-IPF-MEM-1288, European Space Agency, 2016.

Farrell, S. L., McAdoo, D. C., Laxon, S. W., Zwally, H. J., Yi, D., Ridout, A., and Giles, K. A.: Mean dynamic topography of the Arctic Ocean, Geophysical Research Letters, 39, 1–5, https://doi.org/10.1029/2011GL050052, 2012.

Fofonoff, N.P, and Millard, R.C.: Algorithms for computation of fundamental properties of seawater, Tech. rep., https://repository.oceanbestpractices.org/handle/11329/109, 1983.

Fukumori, I., Raghunath, R., and Fu, L. L.: Nature of global large-scale sea level variability in relation to atmospheric forcing: A modeling study, Journal of Geophysical Research: Solid Earth, 103, 5493–5512, https://doi.org/10.1029/97JC02907, 1998.

Fukumori, I., Wang, O., Llovel, W., Fenty, I., and Forget, G.: A near-uniform fluctuation of ocean bottom pressure and sea level across the deep ocean basins of the Arctic Ocean and the Nordic Seas, Progress in Oceanography, 134, 152–172, https://doi.org/10.1016/j.pocean.2015.01.013, 2015.

Giles, K. A., Laxon, S. W., Ridout, A. L., Wingham, D. J., and Bacon, S.: Western Arctic Ocean freshwater storage increased by wind-driven spin-up of the Beaufort Gyre, Nature Geoscience, 5, 194–197, https://doi.org/10.1038/ngeo1379, 2012.

Gruber, T. and Willberg, M.: Signal and error assessment of GOCE-based high resolution gravity field models, Journal of Geodetic Science, 9, 71–86, https://doi.org/10.1515/jogs-2019-0008, 2019.

Hakkinen, S., Proshutinsky, A., and Ashik, I.: Sea ice drift in the Arctic since the 1950s, Geophysical Research Letters, 35, 1 – 5, https://doi.org/10.1029/2008gl034791, 2008.

Haller, M., Brümmer, B., and Müller, G.: Atmosphere–ice forcing in the transpolar drift stream: results from the DAMOCLES ice-buoy campaigns 2007–2009, The Cryosphere, 8, 275–288, https://doi.org/10.5194/tc-8-275-2014, 2014.

Hattermann, T., Isachsen, P. E., von Appen, W.-J., and Sundfjord, A.: Eddy-driven recirculation of Atlantic Water in Fram Strait, Geophysical Research Letters, 43, 3406–3414, https://doi.org/10.1002/(ISSN)1944-8007, 2016.

Hendricks, S., Ricker, R., and Paul, S.: Product User Guide & Algorithm Specification: AWI CryoSat-2 Sea Ice Thickness (version 2.4), EPIC.awi.de, Alfred Wegener Institute Helmholtz Centre for Polar and Marine Research, https://epic.awi.de/id/eprint/54733/, 2021.

Iona, A., Theodorou, A., Watelet, S., Troupin, C., Beckers, J.-M., and Simoncelli, S.: Mediterranean Sea Hydrographic Atlas: towards optimal
data analysis by including time-dependent statistical parameters, Earth System Science Data, 10, 1281–1300, https://doi.org/10.5194/essd-
10-1281-2018, 2018.

Jahn, A., Tremblay, L. B., Newton, R., Holland, M. M., Mysak, L. A., and Dmitrenko, I. A.: A tracer study of the Arctic Ocean's liquid
freshwater export variability, Journal of Geophysical Research: Solid Earth, 115, 10 419, https://doi.org/10.1029/2009JC005873, 2010.

Jakobsson, M., Mayer, L., Coakley, B., Dowdeswell, J. A., Forbes, S., Fridman, B., Hodnesdal, H., Noormets, R., Pedersen, R., Rebesco, M.,
Schenke, H. W., Zarayskaya, Y., Accettella, D., Armstrong, A., Anderson, R. M., Bienhoff, P., Camerlenghi, A., Church, I., Edwards, M.,
Gardner, J. V., Hall, J. K., Hell, B., Hestvik, O., Kristoffersen, Y., Marcussen, C., Mohammad, R., Mosher, D., Nghiem, S. V., Pedrosa,
M. T., Travaglini, P. G., and Weatherall, P.: The International Bathymetric Chart of the Arctic Ocean (IBCAO) Version 3.0, Geophysical
Research Letters, 39, n/a–n/a, https://doi.org/10.1029/2012gl052219, 2012.

Janout, M. A., Aksenov, Y., Hölemann, J. A., Rabe, B., Schauer, U., Polyakov, I. V., Bacon, S., Coward, A. C., Karcher, M., Lenn,
Y.-D., Kassens, H., and Timokhov, L.: Kara Sea freshwater transport through Vilkitsky Strait: Variability, forcing, and further path-
ways toward the western Arctic Ocean from a model and observations, Journal of Geophysical Research: Oceans, 120, 4925–4944,
https://doi.org/10.1002/2014JC010635, 2015.

Kaur, S., Ehn, J. K., and Barber, D. G.: Pan-arctic winter drift speeds and changing patterns of sea ice motion: 1979–2015, Polar Record, 54,
303–311, https://doi.org/10.1017/S0032247418000566, 2018.

Knudsen, P., Andersen, O., and Maximenko, N.: A new ocean mean dynamic topography model, derived from a combination of gravity,
altimetry and drifter velocity data, Advances in Space Research, https://doi.org/https://doi.org/10.1016/j.asr.2019.12.001, 2019.

Komjathy, A. and Born, G. H.: GPS-based ionospheric corrections for single frequency radar altimetry, Journal of Atmospheric and Solar-
Terrestrial Physics, 61, 1197–1203, https://doi.org/10.1016/S1364-6826(99)00051-6, 1999.

Kwok, R. and Morison, J.: Dynamic topography of the ice-covered Arctic Ocean from ICESat, Geophysical Research Letters, 38, 1–6,
https://doi.org/10.1029/2010GL046063, 2011.

Kwok, R. and Morison, J.: Sea surface height and dynamic topography of the ice-covered oceans from CryoSat-2: 2011-2014, Journal of
Geophysical Research: Oceans, 121, 674–692, https://doi.org/10.1002/2015JC011357, 2016.

Kwok, R., Spreen, G., and Pang, S.: Arctic sea ice circulation and drift speed: Decadal trends and ocean currents, Journal of Geophysical
Research: Oceans, 118, 2408–2425, https://doi.org/10.1002/jgrc.20191, 2013.

Landy, J. C., Bouffard, J., Wilson, C., Rynders, S., Aksenov, Y., and Tsamados, M.: Improved Arctic Sea Ice Freeboard Re-
trieval From Satellite Altimetry Using Optimized Sea Surface Decorrelation Scales, Journal of Geophysical Research: Oceans, 126,
https://doi.org/10.1029/2021jc017466, 2021.

Lauvset, S. K., Key, R. M., Olsen, A., Heuven, S. v., Velo, A., Lin, X., Schirnick, C., Kozyr, A., Tanhua, T., Hoppema, M., Jutterström,
S., Steinfeldt, R., Jeansson, E., Ishii, M., Perez, F. F., Suzuki, T., and Watelet, S.: A new global interior ocean mapped climatology: the
1°×1° GLODAP version 2, Earth System Science Data, 8, 325 – 340, https://doi.org/10.5194/essd-8-325-2016, https://essd.copernicus.
org/articles/8/325/2016/, 2016.

Laxon, S. W.: Sea ice altimeter processing scheme at the EODC, International Journal of Remote Sensing, 15, 915–924,
https://doi.org/10.1080/01431169408954124, 1994.

Le Bras, I. A. A., Straneo, F., Holte, J., and Holliday, N. P.: Seasonality of Freshwater in the East Greenland Current System From 2014 to
2016, Journal of Geophysical Research: Oceans, 123, 8828–8848, https://doi.org/10.1029/2018JC014511, 2018.

960   Lenartz, F., Troupin, C., and Lefebvre, W.: Air Pollution Modeling and its Application XXV, Springer Proceedings in Complexity, pp. 231–235, https://doi.org/10.1007/978-3-319-57645-9_37, 2017.

Lyard, F., Lefevre, F., Letellier, T., and Francis, O.: Modelling the global ocean tides: modern insights from FES2004, Ocean Dynamics, 56, 394–415, https://doi.org/10.1007/s10236-006-0086-x, 2006.

Lyard, F. H., Allain, D. J., Cancet, M., Carrère, L., and Picot, N.: FES2014 global ocean tide atlas: design and performance, Ocean Science,

965   17, 615–649, https://doi.org/10.5194/os-17-615-2021, 2021.

Ma, B., Steele, M., and Lee, C. M.: Ekman circulation in the Arctic Ocean: Beyond the Beaufort Gyre, Journal of Geophysical Research: Oceans, 122, 3358–3374, https://doi.org/10.1002/2016JC012624, 2017.

McPhee, M. G.: Intensification of Geostrophic Currents in the Canada Basin, Arctic Ocean, Journal of Climate, 26, 3130–3138, https://doi.org/10.1175/JCLI-D-12-00289.1, 2012.

970   Min, L., Pickart, R. S., Spall, M. A., Weingartner, T. J., Lin, P., Moore, G. W. K., and Qi, Y.: Circulation of the Chukchi Sea shelfbreak and slope from moored timeseries, Progress in Oceanography, 172, 14–33, https://doi.org/10.1016/j.pocean.2019.01.002, 2019.

Mizobata, K., Watanabe, E., and Kimura, N.: Wintertime variability of the Beaufort gyre in the Arctic Ocean derived from CryoSat-2/SIRAL observations, Journal of Geophysical Research: Oceans, 121, 1685–1699, https://doi.org/10.1002/2015JC011218, 2016.

Morgan, P. and Pender, L.: CSIRO MATLAB seawater library., 2009.

975   Morison, J., Kwok, R., Peralta-Ferriz, C., Alkire, M., Rigor, I., Andersen, R., and Steele, M.: Changing Arctic Ocean freshwater pathways, Nature, 481, 66 – 70, https://doi.org/10.1038/nature10705, 2012.

Morison, J., Kwok, R., Dickinson, S., Morison, D., Peralta-Ferriz, C., and Andersen, R.: Sea State Bias of ICESat in the Subarctic Seas, IEEE Geoscience and Remote Sensing Letters, 15, 1144–1148, https://doi.org/10.1109/lgrs.2018.2834362, 2018.

Morison, J., Kwok, R., Dickinson, S., Andersen, R., Peralta-Ferriz, C., Morison, D., Rigor, I., Dewey, S., and Guthrie, J.: The Cyclonic

980   Mode of Arctic Ocean Circulation, Journal of Physical Oceanography, 51, 1053 – 1075, https://doi.org/10.1175/jpo-d-20-0190.1, https://journals.ametsoc.org/view/journals/phoc/51/4/JPO-D-20-0190.1.xml, 2021.

Mulet, S., Rio, M. H., Etienne, H., Artana, C., Cancet, M., Dibarboure, G., Feng, H., Husson, R., Picot, N., Provost, C., and Strub, P. T.: The new CNES-CLS18 Global Mean Dynamic Topography, Ocean Science, pp. 1–31, https://doi.org/10.5194/os-2020-117, 2021.

Müller, F. L., Wekerle, C., Dettmering, D., Passaro, M., Bosch, W., and Seitz, F.: Dynamic Ocean Topography of the Greenland Sea: A

985   comparison between satellite altimetry and ocean modeling, The Cryosphere, p. 611–626, https://doi.org/10.5194/tc-13-611-2019, 2019.

Nurser, A. J. G. and Bacon, S.: The Rossby radius in the Arctic Ocean, Ocean Science, 10, 967–975, https://doi.org/10.5194/os-10-967-2014, 2014.

Passaro, M., Cipollini, P., Vignudelli, S., Quartly, G. D., and Snaith, H. M.: ALES: A multi-mission adaptive subwaveform retracker for coastal and open ocean altimetry, Remote Sensing of Environment, 145, 173–189, https://doi.org/10.1016/j.rse.2014.02.008, 2014.

990   Pawlowicz, R., Beardsley, B., and Lentz, S.: Classical tidal harmonic analysis including error estimates in MATLAB using T_TIDE, Computers & Geosciences, 28, 929–937, https://doi.org/10.1016/S0098-3004(02)00013-4, 2002.

Peralta-Ferriz, C. and Morison, J.: Understanding the annual cycle of the Arctic Ocean bottom pressure, Geophysical Research Letters, 37, 1–6, https://doi.org/10.1029/2010GL042827, 2010.

Peralta-Ferriz, C., Morison, J. H., Wallace, J. M., and Zhang, J.: A basin-coherent mode of sub-monthly variability in Arctic Ocean bottom

995   pressure, Geophysical Research Letters, 38, https://doi.org/10.1029/2011GL048142, 2011.

Pérez Hernández, M. D., Pickart, R. S., Torres, D. J., Bahr, F., Sundfjord, A., Ingvaldsen, R., Renner, A. H. H., Möller, A. B., von Appen, W.-J., and Pavlov, V.: Structure, Transport, and Seasonality of the Atlantic Water Boundary Current North of Svalbard: Results From a Yearlong Mooring Array, Journal of Geophysical Research: Oceans, 124, 1679–1698, https://doi.org/10.1029/2018JC014759, 2019.

Pnyushkov, A. V., Polyakov, I. V., Ivanov, V. V., Aksenov, Y., Coward, A. C., Janout, M., and Rabe, B.: Structure and variability of the boundary current in the Eurasian Basin of the Arctic Ocean, Deep-Sea Research Part I, 101, 80–97, https://doi.org/10.1016/j.dsr.2015.03.001, 2015.

Pnyushkov, A. V., Polyakov, I. V., Padman, L., and Nguyen, A. T.: Structure and dynamics of mesoscale eddies over the Laptev Sea continental slope in the Arctic Ocean, Ocean Science, 14, 1329–1347, https://doi.org/10.5194/os-14-1329-2018, 2018.

Polyakov, I. V.: NABOS II - ADCP Water Current Data 2013 - 2015., Arctic Data Center, https://doi.org/doi:10.18739/A28G8FJ3H, 2016.

Polyakov, I. V.: Acoustic Dopper Current Profiler (ADCP) from moorings taken in the Eurasian and Makarov basins, Arctic Ocean, 2015-2018. , https://doi.org/doi:10.18739/A2HT2GB80, 2019.

Polyakov, I. V. and Rembert, R.: Conductivity, Temperature, Pressure (CTD) measurements from Sea Bird Electronics SBE37 instruments taken in the Eurasian and Makarov basins, Arctic Ocean, 2015-2018., Arctic Data Center, https://doi.org/doi:10.18739/A2NK3652R, 2019.

Ponte, R. M. and Gaspar, P.: Regional analysis of the inverted barometer effect over the global ocean using TOPEX/POSEIDON data and model results, Journal of Geophysical Research, 104, 15 587–15 601, https://doi.org/10.1029/1999JC900113, 1999.

Prandi, P., Poisson, J.-C., Faugère, Y., Guillot, A., and Dibarboure, G.: Arctic sea surface height maps from multi-altimeter combination, Earth System Science Data, 13, 5469–5482, https://doi.org/10.5194/essd-13-5469-2021, 2021.

Proshutinsky, A., Krishfield, R., Timmermans, M.-L., Toole, J., Carmack, E. C., McLaughlin, F., Williams, W. J., Zimmermann, S., Itoh, M., and Shimada, K.: Beaufort Gyre freshwater reservoir: State and variability from observations, Journal of Geophysical Research: Solid Earth, 114, 14 485, https://doi.org/10.1029/2008JC005104, 2009.

Proshutinsky, A. Y. and Johnson, M. A.: Two circulation regimes of the wind-driven Arctic Ocean, Journal of Geophysical Research: Solid Earth, 102, 12 493–12 514, https://doi.org/10.1029/97JC00738, https://agupubs.onlinelibrary.wiley.com/doi/full/10.1029/97JC00738, 1997.

Pujol, M. I., Dobricic, S., Pinardi, N., and Adani, M.: Impact of Multialtimeter Sea Level Assimilation in the Mediterranean Forecasting Model, Journal of Atmospheric and Oceanic Technology, 27, 2065 – 2082, https://doi.org/10.1175/2010jtecho715.1, 2010.

Pujol, M.-I., Faugère, Y., Taburet, G., Dupuy, S., Pelloquin, C., Ablain, M., and Picot, N.: DUACS DT2014: the new multi-mission altimeter data set reprocessed over 20 years, Ocean Science, 12, 1067 – 1090, https://www.ocean-sci.net/12/1067/2016/os-12-1067-2016.pdf, 2016.

Quartly, G. D., Rinne, E., Passaro, M., Andersen, O. B., Dinardo, S., Fleury, S., Guillot, A., Hendricks, S., Kurekin, A. A., Müller, F. L., Ricker, R., Skourup, H., and Tsamados, M.: Retrieving Sea Level and Freeboard in the Arctic: A Review of Current Radar Altimetry Methodologies and Future Perspectives, Remote Sensing, 11, 881, https://doi.org/10.3390/rs11070881, 2019.

Quinn, K. J. and Ponte, R. M.: High frequency barotropic ocean variability observed by GRACE and satellite altimetry, Geophysical Research Letters, 39, 1–5, https://doi.org/10.1029/2012GL051301, 2012.

Rabe, B., Karcher, M., Kauker, F., Schauer, U., Toole, J. M., Krishfield, R. A., Pisarev, S., Kikuchi, T., and Su, J.: Arctic Ocean basin liquid freshwater storage trend 1992–2012, Geophysical Research Letters, 41, 961–968, https://doi.org/10.1002/2013gl058121, 2014.

Ricker, R., Hendricks, S., Helm, V., and Davidson, M.: Sensitivity of CryoSat-2 Arctic sea-ice freeboard and thickness on radar-waveform interpretation, The Cryosphere, 8, 1607–1622, https://doi.org/10.5194/tc-8-1607-2014, 2014.

Ricker, R., Hendricks, S., and Beckers, J.: The Impact of Geophysical Corrections on Sea-Ice Freeboard Retrieved from Satellite Altimetry, Remote Sensing, 8, 1–15, https://doi.org/10.3390/rs8040317, 2016.

1035   Rio, M. H., Guinehut, S., and Larnicol, G.: New CNES-CLS09 global mean dynamic topography computed from the combination of GRACE data, altimetry, and in situ measurements, Journal of Geophysical Research, 116, C11 001–25, https://doi.org/10.1029/2010JC006505, 2011.

Rixen, M., Beckers, J. M., Brankart, J. M., and Brasseur, P.: A numerically efficient data analysis method with error map generation, Ocean Modelling, 2, 45 – 60, https://doi.org/10.1016/s1463-5003(00)00009-3, https://www.sciencedirect.com/science/article/abs/
1040   pii/S1463500300000093, 2000.

Robbins, J. W., Neumann, T. A., Kwok, R., and Morison, J.: ICESat-2 Oceanic & Sea Ice Responses to Atmospheric Forcing, 2016 Fall meeting, AGU, San Francisco, CA, 12-16 Dec., https://ui.adsabs.harvard.edu/abs/2016AGUFM.C11A0744R/abstract, 2016.

Rose, S. K., Andersen, O. B., Passaro, M., Ludwigsen, C. A., and Schwatke, C.: Arctic Ocean Sea Level Record from the Complete Radar Altimetry Era: 1991–2018, Remote Sensing, 11, 1672, https://doi.org/10.3390/rs11141672, 2019.

1045   Scharroo, R. and Lillibridge, J.: Non-Parametric Sea-State Bias Models and Their Relevance to Sea Level Change Studies, in: Envisat ERS Symposium, Salzburg, Austria, 2005.

Scharroo, R., Leuliette, E., Lillibridge, J., Byrne, D., Naeije, M., and Mitchum, G.: RADS: Consistent multi-mission products, in: Proc. of the Symposium on Years of Progress in Radar Altimetry, Venice, - September, Eur. Space Agency Spec. Publ., 2013.

Scharroo, Remko: RADS data manual., Tech. rep., https://usermanual.wiki/Document/rads4datamanual.1752171340/help, 2018.

1050   Schauer, U., Loeng, H., Rudels, B., Ozhigin, V. K., and Dieck, W.: Atlantic Water flow through the Barents and Kara Seas , Deep-Sea Research Part I, https://doi.org/10.1016/S0967-0637(02)00125-5, 2002.

Siegismund, F., Johannessen, J., Drange, H., Mork, K. A., and Korablev, A.: Steric height variability in the Nordic Seas, Journal of Geophysical Research: Solid Earth, 112, 2733, https://doi.org/10.1029/2007JC004221, 2007.

Solomon, A., Heuzé, C., Rabe, B., Bacon, S., Bertino, L., Heimbach, P., Inoue, J., Iovino, D., Mottram, R., Zhang, X., Aksenov, Y.,
1055   McAdam, R., Nguyen, A., Raj, R. P., and Tang, H.: Freshwater in the Arctic Ocean 2010–2019, Ocean Science, 17, 1081–1102, https://doi.org/10.5194/os-17-1081-2021, 2021.

Spreen, G., Kwok, R., and Menemenlis, D.: Trends in Arctic sea ice drift and role of wind forcing: 1992-2009, Geophysical Research Letters, 38, 1–6, https://doi.org/10.1029/2011GL048970, 2011.

Stammer, D., Wunsch, C., and Ponte, R. M.: De-aliasing of global high frequency barotropic motions in altimeter observations, Geophysical
1060   Research Letters, 27, 1175–1178, https://doi.org/10.1029/1999GL011263, 2000.

Timmermans, M.-L. and Marshall, J.: Understanding Arctic Ocean Circulation: A Review of Ocean Dynamics in a Changing Climate, Journal of Geophysical Research: Oceans, 125, C04S02, https://doi.org/10.1029/2018jc014378, https://agupubs.onlinelibrary.wiley.com/doi/epdf/10.1029/2018JC014378, 2020.

Troupin, C., Machín, F., Ouberdous, M., Sirjacobs, D., Barth, A., and Beckers, J. M.: High-resolution climatology of the north-
1065   east Atlantic using Data-Interpolating Variational Analysis (Diva), Journal of Geophysical Research: Solid Earth, 115, 455, https://doi.org/10.1029/2009jc005512, 2010.

Troupin, C., Barth, A., Sirjacobs, D., Ouberdous, M., Brankart, J. M., Brasseur, P., Rixen, M., Alvera-Azcárate, A., Belounis, M., Capet, A., Lenartz, F., Toussaint, M. E., and Beckers, J. M.: Generation of analysis and consistent error fields using the Data Interpolating Variational Analysis (DIVA), Ocean Modelling, 52-53, 90–101, https://doi.org/10.1016/j.ocemod.2012.05.002, 2012.

1070 Tyberghein, L., Verbruggen, H., Pauly, K., Troupin, C., Mineur, F., and Clerck, O. D.: Bio-ORACLE: a global environmental dataset for marine species distribution modelling, Global Ecology and Biogeography, 21, 272 – 281, https://doi.org/10.1111/j.1466-8238.2011.00656.x, https://onlinelibrary.wiley.com/doi/full/10.1111/j.1466-8238.2011.00656.x, 2012.

Vinogradova, N. T., Ponte, R. M., and Stammer, D.: Relation between sea level and bottom pressure and the vertical dependence of oceanic variability, Geophysical Research Letters, 34, C03 010, https://doi.org/10.1029/2006GL028588, 2007.

1075 Volkov, D. L. and Pujol, M. I.: Quality assessment of a satellite altimetry data product in the Nordic, Barents, and Kara seas, Journal of Geophysical Research, 117, 1–12, https://doi.org/10.1029/2011JC007557, 2012.

Volkov, D. L., Landerer, F. W., and Kirillov, S. A.: The genesis of sea level variability in the Barents Sea, Continental Shelf Research, 66, 92–104, https://doi.org/10.1016/j.csr.2013.07.007, 2013.

von Appen, W.-J.: Physical oceanography and current meter data (including raw data) from FRAM moorings in the Fram Strait, 2016-2018,
1080 PANGAEA, https://doi.org/10.1594/PANGAEA.904565, 2019.

von Appen, W.-J., Schauer, U., Somavilla Cabrillo, R., Bauerfeind, E., and Beszczynska-Möller, A.: Physical oceanography during various cruises to the Fram Strait, 1998-2012, PANGAEA, https://doi.org/10.1594/PANGAEA.150007, https://doi.org/10.1594/PANGAEA. 150007, in supplement to: von Appen, Wilken-Jon; Schauer, Ursula; Somavilla, Raquel; Bauerfeind, Eduard; Beszczynska-Möller, Agnieszka (2015): Exchange of warming deep waters across Fram Strait. Deep Sea Research Part I: Oceanographic Research Papers, 103,
1085 86-100, https://doi.org/10.1016/j.dsr.2015.06.003, 2015.

von Appen, W.-J., Schauer, U., Hattermann, T., and Beszczynska-Möller, A.: Seasonal Cycle of Mesoscale Instability of the West Spitsbergen Current, Journal of Physical Oceanography, 46, 1231–1254, https://doi.org/10.1175/JPO-D-15-0184.1, 2016.

von Appen, W.-J., Beszczynska-Möller, A., Schauer, U., and Fahrbach, E.: Physical oceanography and current meter data from moorings F1-F14 and F15/F16 in the Fram Strait, 1997-2016, PANGAEA, https://doi.org/10.1594/PANGAEA.900883, 2019.

1090 Wahr, J. M.: Deformation induced by polar motion, Journal of Geophysical Research: Solid Earth, 90, 9363–9368, https://doi.org/10.1029/JB090iB11p09363, 1985.

Watelet, S., Skagseth, Ø., Lien, V. S., Sagen, H., Østensen, Ø., Ivshin, V., and Beckers, J.-M.: A volumetric census of the Barents Sea in a changing climate, Earth System Science Data, 12, 2447 – 2457, https://doi.org/10.5194/essd-12-2447-2020, https://essd.copernicus.org/articles/12/2447/2020/essd-12-2447-2020.html, 2020.

1095 Willmes, S. and Heinemann, G.: Sea-Ice Wintertime Lead Frequencies and Regional Characteristics in the Arctic, 2003–2015, Remote Sensing, 8, 4, https://doi.org/10.3390/rs8010004, 2016.

Wingham, D. J., Francis, C. R., Baker, S., Bouzinac, C., Brockley, D., Cullen, R., de Chateau-Thierry, P., Laxon, S. W., Mallow, U., Mavrocordatos, C., Phalippou, L., Ratier, G., Rey, L., Rostan, F., Viau, P., and Wallis, D. W.: CryoSat: A mission to determine the fluctuations in Earth's land and marine ice fields , Advances in Space Research, 37, 841–871, https://doi.org/10.1016/j.asr.2005.07.027, 2006.